TU Delft

Delft University of Technology

Interoperability of classical and advanced controllers in MMC based MTDC power system

Liu, L.; Shetgaonkar, A.D.; Lekic, A.

DOI
10.1016/j.ijepes.2023.108980

Publication date
2023

Document Version
Final published version

Published in
International Journal of Electrical Power & Energy Systems

Citation (APA)
Liu, L., Shetgaonkar, A. D., & Lekic, A. (2023). Interoperability of classical and advanced controllers in MMC based MTDC power system. *International Journal of Electrical Power & Energy Systems*, *148*(108980), Article 108980. https://doi.org/10.1016/j.ijepes.2023.108980

Important note
To cite this publication, please use the final published version (if applicable).
Please check the document version above.

Copyright
Other than for strictly personal use, it is not permitted to download, forward or distribute the text or part of it, without the consent of the author(s) and/or copyright holder(s), unless the work is under an open content license such as Creative Commons.

Takedown policy
Please contact us and provide details if you believe this document breaches copyrights.
We will remove access to the work immediately and investigate your claim.

This work is downloaded from Delft University of Technology.
For technical reasons the number of authors shown on this cover page is limited to a maximum of 10.

Electrical Power and Energy Systems 148 (2023) 108980

Contents lists available at ScienceDirect

International Journal of Electrical Power and Energy Systems

journal homepage: www.elsevier.com/locate/ijepes

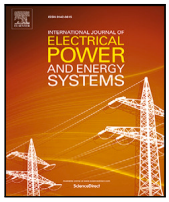

Interoperability of classical and advanced controllers in MMC based MTDC power system

Le Liu *, Ajay Shetgaonkar, Aleksandra Lekić

Intelligent Electrical Power Grids (IEPG-ESE), TU Delft, Delft, The Netherlands

ARTICLE INFO

Keywords:
Interoperability
MMC non-linear control
MTDC system
MPC
Back-stepping control
Sliding-mode control
RTDS
Power system transients

ABSTRACT

This paper presents the modular-multilevel-converter (MMC) control interoperability (IOP) and interaction within the High Voltage Direct Current (HVDC)-based power system. IOP is a crucial issue in the large-scale HVDC grid with different suppliers. To accommodate future multi-vendor HVDC grids developments, this article comprehensively investigates the MMC control IOP issue. Firstly, the most commonly adopted proportional-integral (PI) control and other non-linear controllers, e.g., model predictive control (MPC), back-stepping control (BSC), and sliding mode control (SMC), are constructed for MMC. Then, the IOP simulations are carried out in a multi-terminal direct current (MTDC) system in real-time digital simulator (RTDS) environment. The most frequent transients of the practical projects, e.g., power flow changing, wind speed changing, and DC/AC grid faults, are simulated with eight different scenarios. Each scenario presents different control capabilities in maintaining system stability, more precisely, the scenarios with non-linear controllers show faster settling time and fewer DC voltage and power variations. Controller switchings are also achieved without bringing large system oscillations. This paper provides the optimal allocation strategy of controllers to cope with system transients.

1. Introduction

In the near future, multi-technology installations will be part of the large-scale (multi-gigawatt) windfarm tenders, including multi-vendor converter stations. Hence, technological and manufacturer interoperability will be required for an uninterrupted electricity supply. In recent years, researchers have proposed various advanced MMC controllers to enhance the performance of classical MMC controls. However, there is a lack of MMC control standardization, and the majority of HVDC projects are constructed in a vendor-specific manner. To this date, it is unknown how the power electronic converters from different manufacturers will interoperate, and which information should be exchanged between control and protection units. Different possible forms of operational incompatibility of different MMC technologies constitute unprecedented phenomena that have been reported in a few recent preliminarily studies [1]. One of the initially studied aspects is the dynamic interplay between half/full-bridge MMC units belonging to a MTDC power systems [2]. In Rault et al. [3] is reported a slower abnormal oscillation due to a multi-vendor voltage source converter's (VSC's) interaction, which is damped by DC voltage control. Field/numerical simulation-based experiments are presented in Ansari et al. [4], discussing how converters with different dispatch and upper-level controls interact with each other. So far, there have been conducted multi-vendor protection studies [5]. Furthermore, projects Best Paths [6] and PROMOTioN [7] have given a good basis for the multi-vendor control and protection studies, which are currently being extended by READY4DC and InterOPERA projects.

In this paper we will provide detailed models for the three terminal MTDC for the control interoperability study. In their design, the ratings for the upcoming ±525 kV, 2 GW connections have been used. These models are filling in the gap that is not covered by recent CIGRE brochures [8,9]. Lower bandwidth of the outer voltage control of converter has a significant impact on the rotor angle stability during small-disturbance. Also, this controlling loop greatly influences voltage stability [10]. Similarly, the inner current control loop causes fast-interaction converter-driven stability problems. These issues can be mitigated by making use of non-linear controllers. However, a thorough assessment of the performance of the different controllers of the MMC units, interacting through an MTDC, by using detailed models, is an acknowledged scientific gap. The emphasis of the presented research work is on a comprehensive assessment of the interaction of the MMC units' inner and outer control functions under classical

* Corresponding author.
E-mail address: L.Liu-7@tudelft.nl (L. Liu).

https://doi.org/10.1016/j.ijepes.2023.108980
Received 26 September 2022; Received in revised form 20 December 2022; Accepted 14 January 2023
Available online 20 January 2023
0142-0615/© 2023 The Author(s). Published by Elsevier Ltd. This is an open access article under the CC BY license (http://creativecommons.org/licenses/by/4.0/).

PI methods in Bergna-Diaz et al. [11], and non-linear control methods [12]. The controller interoperability study are analyzed following non-linear control methods:

- Model Predictive Control (MPC) has been known for the last 20 years in mechanical and aerospace applications. The Multiple Input Multiple Output (MIMO) characteristics, robust and fast response made these algorithms popular in power electronic applications. In power electronic applications, the MPC is classified into two major categories; Direct and indirect MPC [13–15]. This classification is made based on the presence or absence of a modulator. In literature, the majority of indirect MPC has been investigated for HVDC - MMC application in offline simulations. Thus dependence on time is removed. Further, there are few research on the MPC-based MMC- MTDC system and the interaction of MPC with different control has not been analyzed.
- Back-Stepping Control (BSC) has a systematic and recursive design methodology, which links the design of Lyapunov function with a feedback controller and ensures global asymptotic stability. The BSC approaches outlined in Ahmadijokani et al. [16] and Jin et al. [17] utilize the energy controller to deliver the set-point to the grid current controller. A disturbance-tracking-based backstepping control is proposed in Liu et al. [18]. However, the feasibility of aforementioned methods in MTDC system needs further investigation. The authors of Zhao and Li [19] designed the BSC method based on the simplified transmission model, and the interaction of wind farms is also considered. However, due to the imprecision of the model, the control's effectiveness needs to be further verified.
- The Sliding Mode Control (SMC) has the merits of high robustness against system uncertainties and prompt transient response. Recently, the second-order SMC (SOSMC) became popular since it not only preserves the robustness properties of the classical SMC, but also overcomes the shortcomings of high-frequency chattering and infinite time convergence, of which the most feasible solutions for practical projects are the twisting controller and super-twisting sliding mode controllers (STSMC) [20,21]

Since the control settling interoperability of MMC based MTDC system has not been achieved previously, this article presents the first study on the interoperability study of various controllers in the MMC based MTDC system, which has profound significance for the switching and cooperation between different MMC controllers in practical MTDC engineering. Firstly, this article presents the general MMC dynamics behaviors, designs of classical and advanced nonlinear controllers. Then, this article reports the IOP simulation results with most commonly occurred system transients in RTDS and hardware-in-the-loop (HIL) testing environments. Experimental results prove that properly designing and tuning these advanced controllers makes it possible to achieve the IOP between different controllers in the multi-vendor MTDC system. Besides, these non-linear controllers operate without a significant ripple, which is much more robust than the conventional PI.

The rest of this paper is structured as follows. Section 2 presents a brief introduction of the typical configuration and dynamic behaviors of the MMC converter. Section 3 illustrates the classical PI and advanced controllers design for MMC. Section 4 introduces the studied MTDC system, including the GTFPGA units settling, offshore-windfarms, DC protection, and circuit breakers. Section 5 presents the validation results of the implemented controllers IOP issue through various system transients. Finally concluding remarks along with future work are discussed in Section 6.

2. MMC dynamic behavior

In this section, the MMC and its state-space modeling will be introduced in detail.

2.1. Modeling of MMC

Recently, the MMC has become the most used topology for HVDC applications due to its fast and efficient energy conversion. As a basis for the MMC model, the classical MMC configuration is briefly recalled in Fig. 1, and the stationary reference frame using vector representation is introduced. In Fig. 1, two identical arms are connected to the upper (denoted as U) and lower (denoted as L) arms, forming one leg of each phase $j \in \{a, b, c\}$. N represents the number of half-bridge submodules (SMs) of each arm, and the L_{arm} and R_{arm} denote the equivalent series arm inductance and resistance,respectively. The AC-side interface is assumed as an equivalent resistance and inductance, denoted as R_r and L_r, respectively. Each half-bridge SM consists of four semiconductor switches (S_1, S_2, D_1, D_2) with an anti-paralleled capacitor, of which the voltage is recorded as $v_{Cj}^{U,L}$. Sub-modules are considered with their average equivalents, and thus, the modulated currents $i_{Mj}^{U,L}$ and voltages $v_{Mj}^{U,L}$ of the upper and lower arm of a generic phase j, are here given as follows:

$$v_{Mj}^{U,L} = m_j^{U,L} \cdot v_{Cj}^{U,L}, \qquad i_j^{U,L} = m_j^{U,L} \cdot i_{Cj}^{U,L} \tag{1}$$

where $m_j^{U,L}$ are called the modulation indices of the upper and lower arms for all three phases. Values $v_{Cj}^{U,L}$ and $i_{Cj}^{U,L}$ refer to the voltages and currents of the equivalent capacitance in upper and lower arm.

2.2. State-space modeling in $\Sigma - \Delta$ representation

As mentioned before, the state-space modeling adopted in this work uses the $\Sigma - \Delta$ representation instead of commonly used Upper-Lower form. For the MMC configuration in Fig. 1, the $\Sigma - \Delta$ variables in the upper and lower arms can be presented as follows:

$$v_{Cj}^{\Delta} = \left(v_{Cj}^{U} - v_{Cj}^{L}\right)/2, \qquad v_{Cj}^{\Sigma} = \left(v_{Cj}^{U} + v_{Cj}^{L}\right)/2, \tag{2a}$$

$$m_j^{\Delta} = m_j^{U} - m_j^{L}, \qquad m_j^{\Sigma} = m_j^{U} + m_j^{L}, \tag{2b}$$

$$v_{Mj}^{\Delta} = \left(-v_{Mj}^{U} + v_{Mj}^{L}\right)/2 = -\left(m_j^{\Delta} v_{Cj}^{\Sigma} + m_j^{\Sigma} v_{Cj}^{\Delta}\right)/2, \tag{2c}$$

$$v_{Mj}^{\Sigma} = \left(v_{Mj}^{U} + v_{Mj}^{L}\right)/2 = \left(m_j^{\Sigma} v_{Cj}^{\Sigma} + m_j^{\Delta} v_{Cj}^{\Delta}\right)/2. \tag{2d}$$

Then, the AC gird current dynamics i_j^{Δ} and MMC circulating currents i_j^{Σ} for three-phase case can be defined as:

$$i_j^{\Delta} = i_j^{U} - i_j^{L}, \qquad i_j^{\Sigma} = \left(i_j^{U} + i_j^{L}\right)/2. \tag{3}$$

Using the Kirchhoff voltage law (KVL) in the MMC equivalent circuit depicted in Fig. 1, one can immediately obtain the grid current and circulating current dynamics as:

$$L_{eq}^{ac} \frac{d}{dt}\left(\vec{i}_j^{\Delta}\right) = \vec{v}_{Mj}^{\Delta} - R_{eq}^{ac} \vec{i}_j^{\Delta} - \vec{v}_j^{G}, \tag{4a}$$

$$L_{arm} \frac{d}{dt}\left(\vec{i}_j^{\Sigma}\right) = \frac{v_{dc}}{2} - \vec{v}_{Mj}^{\Sigma} - R_{arm} \vec{i}_j^{\Sigma}, \tag{4b}$$

where, L_{eq}^{ac} and R_{eq}^{ac} are the equivalent inductance and resistance in the AC grid, which are calculated by $L_{eq}^{ac} = L_{arm}/2 + L_r$ and $R_{eq}^{ac} = R_{arm}/2 + R_r$, respectively. $\vec{v}_{Mj}^{\Delta}$ is the modulated voltage at the interfacing point between MMC and AC-grid side and $\vec{v}_j^{G}$ is the three phase AC grid voltage. It is worthwhile mentioning that the Δ variables are associated with the fundamental angular frequency ω, and the third harmonic 3ω components. In comparison, the Σ variables are associated with -2ω harmonics and contain a DC component.

After applying Park's transformation, the grid currents $\vec{i}_{dq}^{\Delta}$ and circulating currents $\vec{i}_{dq}^{\Sigma}$ dynamics can be defined as:

$$\frac{d}{dt}\left(\vec{i}_{dq}^{\Delta}\right) = \frac{1}{L_{eq}^{ac}}\left(\vec{v}_{Mdq}^{\Delta} - \left(\omega L_{eq}^{ac} J_2 + R_{eq}^{ac} I_2\right)\vec{i}_{dq}^{\Delta} - \vec{v}_{dq}^{G}\right), \tag{5a}$$

$$\frac{d}{dt}\left(\vec{i}_{dq}^{\Sigma}\right) = -\frac{1}{L_{arm}}\left(\vec{v}_{Mdq}^{\Sigma} + \left(R_{arm} I_2 - 2\omega L_{arm} J_2\right)\vec{i}_{dq}^{\Sigma}\right), \tag{5b}$$

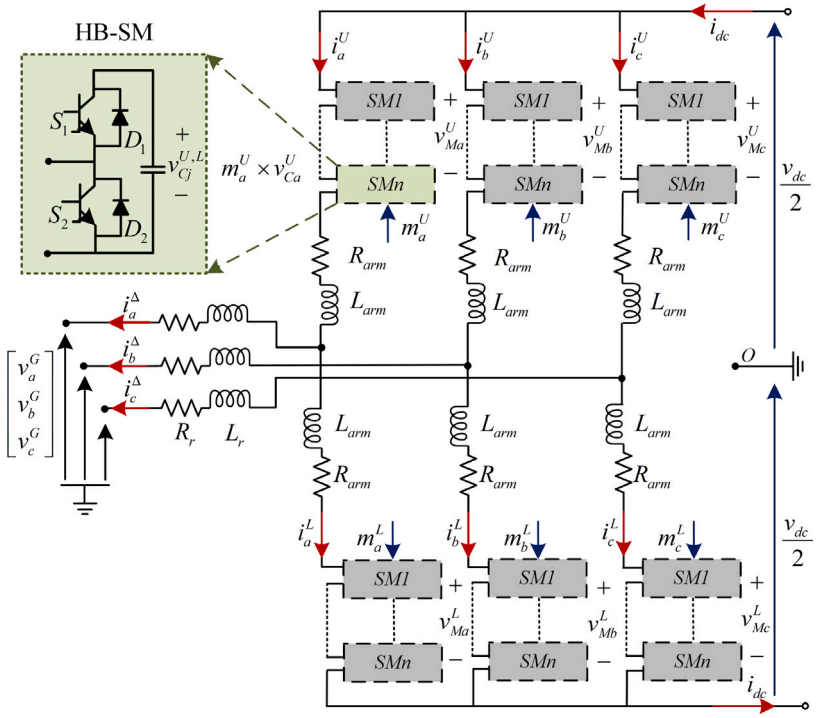

Fig. 1. Schematic diagram of MMC.

where, $\vec{v}^{\Delta}_{Mdq}$ and $\vec{v}^{\Sigma}_{Mdq}$ are the modulated voltages in grid current and circulating current controller, respectively. I_2 is the identity matrix with size 2×2, and $J_2 = \begin{bmatrix} 0 & 1 \\ -1 & 0 \end{bmatrix}$.

3. MMC control formulation

This section presents the detailed MMC modeling process using classical PI control, and advanced MPC, BSC, STSMC control methods.

3.1. PI control formulation

The upper and lower controls of MMCs are based on the PI control published in Cigre B4.57 [22]. Inner current and outer controls depend on the operating mode of the MMC in the MTDC system. Here, MMC1 and MMC3 are grid-following mode, and MMC2 is grid-forming mode. The overall PI control schemes for MMC1,MM2 and MMC3 can be described as follows. The Fig. 2(a) and (b) describe the grid-following control for MMC1 and MMC3, Fig. 2(c) introduces the grid-forming control for MMC2, Fig. 2(d) illustrates the CCSC controller, Fig. 2(e) explains the final modulation indices generation control, the modulated indices are produced for each SMs.

3.1.1. Outer control loops

In case of grid-following MMC1 and MMC3, the outer control loops are generally adopting the DC voltage/active power control to provide the reference signal: $i^{\Delta}_{d,ref}$ for the d-axis grid current, depending on the variation of v_{dc} or P_{ac}, which can be seen as,

$$\dot{\xi}_{v_{dc}} = v_{dc,ref} - v_{dc}, i^{\Delta}_{d,ref} = -K_{P,v_{dc}}\left(v_{dc,ref} - v_{dc}\right) - K_{I,v_{dc}}\xi_{v_{dc}}, \tag{6a}$$

$$\dot{\xi}_P = P_{ac,ref} - P_{ac} i^{\Delta}_{d,ref} = K_{P,P_{ac}}\left(P_{ac,ref} - P_{ac}\right) + K_{I,P_{ac}}\xi_P \tag{6b}$$

where the $K_{P,I,v_{dc}}$ and $K_{P,I,P_{ac}}$ are the control gains of the DC voltage and active power controllers, respectively.

For the reference value $i^{\Delta}_{q,ref}$ of the q-axis grid current, the variation of Q_{ac} or v_{ac} of AC gird can be utilized as:

$$\dot{\xi}_Q = Q_{ac,ref} - Q_{ac}, i^{\Delta}_{q,\mathrm{ref}} = -K_{P,Q_{ac}}\left(Q_{ac,ref} - Q_{ac}\right) + K_{I,Q_{ac}}\xi_Q \tag{7a}$$

$$\dot{\xi}_{v_{ac}} = v_{ac,ref} - v_{ac}, i^{\Delta}_{q,ref} = -K_{P,v_{ac}}\left(v_{ac,ref} - v_{ac}\right) - K_{I,v_{ac}}\xi_{v_{ac}} \tag{7b}$$

where the $K_{P,I,Q_{ac}}$ and $K_{P,I,v_{ac}}$ are the control gains of the reactive power and AC voltage controller.

3.1.2. Output grid current control (OGCC) loops

The OGCC transfers the information about the active power/DC voltage, and reactive power/AC voltage into modulation signals for generating the switching pluses. The OGCC sets the output currents to their reference values provided by the outer control loops $\vec{i}^{\Delta}_{dq,ref}$. This control methods adopt the equations of:

$$\dot{\vec{\xi}}^{\Delta}_{dq} = \vec{i}^{\Delta}_{dq,ref} - \vec{i}^{\Delta}_{dq}, \tag{8a}$$

$$\vec{v}^{\Delta}_{Mdq,ref} = K^{\Delta}_{I,dq}\vec{\xi}^{\Delta}_{dq} + K^{\Delta}_{P,dq}\left(\vec{i}^{\Delta}_{dq,ref} - \vec{i}^{\Delta}_{dq}\right) + \omega L^{ac}_{eq} J_2 \vec{i}^{\Delta}_{dq} + \vec{v}^{G}_{dq}, \tag{8b}$$

where the $K^{\Delta}_{P,I,dq}$ are the control gains for the OGCC controllers. For the offshore MMC2, it is controlled via grid forming control to support wind turbine based on the direct Voltage (V_{ac}/f) control [23], which can be described in the following equations:

$$\dot{\xi}_{v_{ac}} = v_{ac,ref} - v_{ac}, \tag{9a}$$

$$v^{\Delta}_{Md,ref} = K_{I,gf}\xi_{v_{ac}} + K_{P,gf}\dot{\xi}_{v_{ac}} + v_{dc}, v^{\Delta}_{Mq,ref} = 0, \tag{9b}$$

where the $K_{P,gf}$ and $K_{I,gf}$ are the control gains for the grid forming controller.Further, Eq. (9) is applied to the inverse dq-transformation to obtain a three-phase modulating waveform. Due to the absence of the offshore grid reference, we need a self-synchronization mechanism. Hence, an oscillator is used, which provides an angle θ for the inverse dq-transformation.

3.1.3. Circulating current suppression control (CCSC) loops

Difference between the arm phases of the MMC produces a second harmonic circulating current. This current causes voltage ripples in the SM and distorts current through arm. As a result, influences the rating of SM capacitance and IGBT switches. The presence of circulating current suppression control minimizes this effect. The CCSC is constructed to set the circulating currents to their reference values,

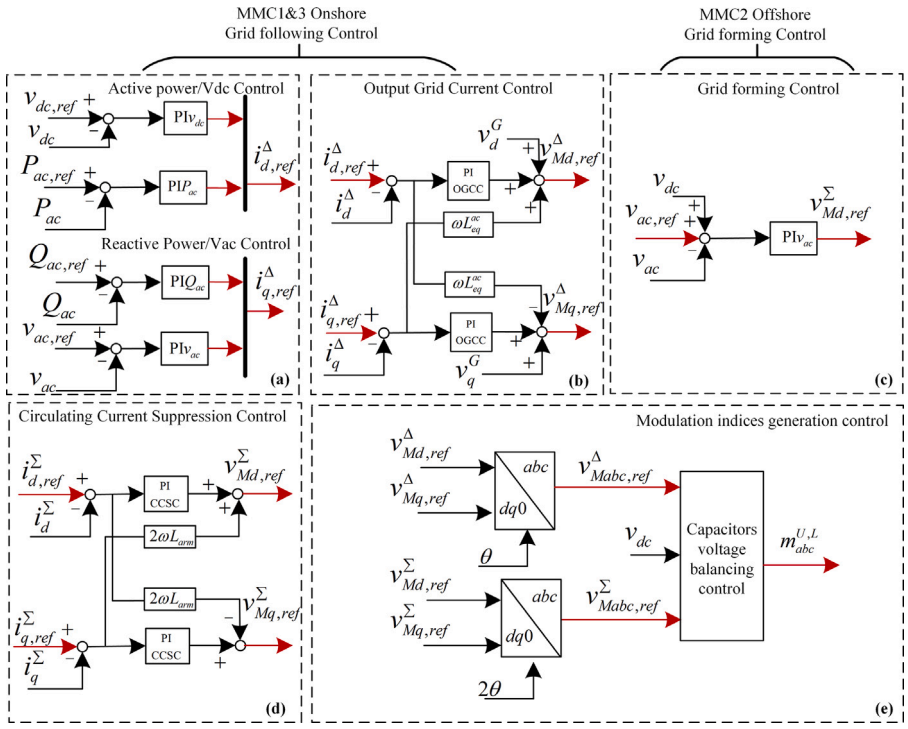

Fig. 2. PI control scheme. (a) Outer control loop. (b) OGCC loop. (c) grid-forming control. (d) CCSC loop. (e) modulation indices generation control.

Table 1
PI control loop parameters [22,24].

V_{dc}	$K_{P,v_{dc}} = 10.0$ $K_{I,v_{dc}} = 5.0$	V_{ac}	$K_{P,v_{ac}} = 1.0$ $K_{I,v_{ac}} = 10.0$
$OGCC_d$	$K^{\Delta}_{P,d} = 0.48$ $K^{\Delta}_{I,d} = 149.25$	$CCSC$	$K^{\Sigma}_{P} = 0.8$ $K^{\Sigma}_{I} = 100.0$
$OGCC_q$	$K^{\Delta}_{P,q} = 0.48$ $K^{\Delta}_{I,q} = 149.25$	Q_{ac}	$K_{P,Q_{ac}} = 1.0$ $K_{I,Q_{ac}} = 33.0$
P_{ac}	$K_{P,P_{ac}} = 0.0$ $K_{I,P_{ac}} = 33.0$	V_{ac}/f	$k_{P,gf} = 1.0$ $K_{I,gf} = 10.0$

which are assumed to be $\vec{i}^{\Sigma}_{dq,ref} = [0, 0]^T$. The specific equations of CCSC adopted are presented as follows,

$$\dot{\vec{\xi}}^{\Sigma}_{dq} = \vec{i}^{\Sigma}_{dq,ref} - \vec{i}^{\Sigma}_{dq}, \tag{10a}$$

$$\vec{v}^{\Sigma}_{Mdq,ref} = -K^{\Sigma}_{I}\vec{\xi}^{\Sigma}_{dq} - K^{\Sigma}_{P}\left(\vec{i}^{\Sigma}_{dq,ref} - \vec{i}^{\Sigma}_{dq}\right) + 2\omega L_{arm} J_2 \vec{i}^{\Sigma}_{dq}, \tag{10b}$$

where K^{Σ}_{p} and K^{Σ}_{I} are the control gains of CCSC loop. The Table 1 lists the control gains of each control loop in our system.

3.2. Model predictive control formulation

The MPC is implemented for two cascaded controllers: inner and outer loop. Inner loop MPC is used to control MMC's currents, while the output loop sets DC voltage. The plant is discretized using the zero-order hold discretization method [12] using an exact solution of the differential equations. Upon discretization, the system is defined with difference equations $\vec{x}(k+1) = A_d\vec{x}(k) + B_d\Delta\vec{u}(k)$, with state variables $\vec{x}$, inputs $\vec{u}$, for kth instance. Matrices A_d and B_d represent the discrete state and input matrices. The continuous state and input matrices for respective loops are defined in Sections 3.2.1 and 3.2.2. Inputs $\Delta\vec{u}(k)$ are represented using orthonormal Laguerre functions [12]. In orthonormal Laguerre functions, the removal of the dependency on the control horizon gives an advantage for real-time applications, as the number of parameters is reduced. With Laguerre's function, the control parameter changes to $\vec{\eta}$ from $\Delta\vec{u}(k)$:

$$\Delta\vec{u}(k+m|k) = \begin{bmatrix} L_1(m)^T & o_1^T & \cdots & o_M^T \\ o_1^T & L_2(m)^T & \cdots & o_M^T \\ \vdots & \vdots & \ddots & \vdots \\ o_1^T & o_2^T & \cdots & L_M(m)^T \end{bmatrix}\vec{\eta}, \tag{11a}$$

$$L(k+1) = A_l L(k), \tag{11b}$$

$$A_l = \begin{bmatrix} a & 0 & 0 & 0 \\ \beta & a & 0 & 0 \\ -a\beta & \beta & a & 0 \\ \vdots & \vdots & \vdots & \ddots \end{bmatrix}, \tag{11c}$$

$$L(0) = \sqrt{\beta}\begin{bmatrix} 1 & -a & a^2 & \cdots & (-1)^{N-1}a^{N-1} \end{bmatrix}, \tag{11d}$$

$$\vec{\eta} = \begin{bmatrix} c_1 & c_2 & \cdots & c_N \end{bmatrix}^T, \tag{11e}$$

where o_k^T represents zero block raw vector with an identical dimension to $L_k(m)^T$. Matrix $L(k) = [l_1(k), l_2(k), \ldots, l_N(k)]^T$, and $l_i(k)$ is the discrete Laguerre function determined using the inverse z transformation of $\Gamma_i(z)$. Function in z domain $\Gamma(z)$ is defined as $\Gamma_i(z) = \Gamma_{i-1}(z)\frac{z^{-1}-a}{1-az^{-1}}$, and $\Gamma_1(z) = \frac{\sqrt{1-a^2}}{1-az^{-1}}$. Here, a is called Laguerre's network pole with a value $0 < a < 1$ for safeguarding the network's stability, $\beta = \sqrt{1-a^2}$, and N is the number of terms required to represent the approximate system response. Notation $\vec{f}(k+m|k)$ denotes discrete value of the vector $\vec{f}$ at the instance $k+m$ estimated during sampling instance k.

The value of η is calculated by minimizing the objective (cost) function, subject to equality and inequality constraints. The cost function is formulated considering the Linear Quadratic Regulator (LQR) as a base. Hence, the cost function is given by

$$\min_{\vec{\eta}} J = \sum_{m=1}^{N_p} \vec{x}(k+m|k)^T Q\vec{x}(k+m|k) + \vec{\eta}^T R\vec{\eta}, \tag{12a}$$

subject to $M\vec{\eta} \le b$, (12b)

$$\vec{x}(k+m|k) = \vec{r}(k) - \vec{y}_m(k+m|k), \tag{12c}$$

where $Q \succeq 0$ and $R \succ 0$ are weighting matrices, and N_p is the prediction horizon. The terminal constraint $\vec{x}(k+N_p|k)$ is set to = 0.

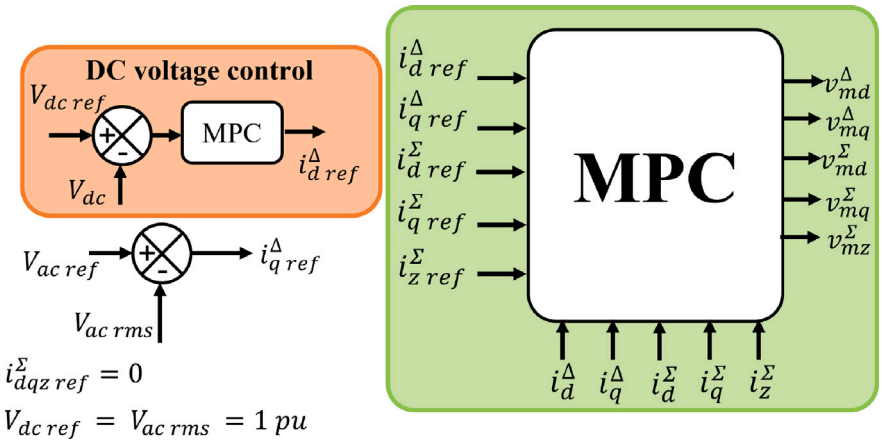

Fig. 3. Graphical representation of MPC formulation.

For variables $\vec{x}(k)$, vector $r(k)$ is a reference signal. The matrix M and vector b correspond to constraint information on rate and amplitude as given [25]. Further, the value of input rate and constraints are given by:

$$\begin{aligned} \Delta U_{max} &= 0.3 \times \vec{1}, \quad \Delta U_{min} = 0.3 \times \vec{1} \\ U_{max} &= 0.8 \times \vec{1}, \quad\quad U_{min} = 0.3 \times \vec{1} \end{aligned} \tag{13}$$

where $\vec{1}$ is vector of all ones.

The quadratic programming problem (12) is solved by making use of Hildreth's quadratic programming procedure [26]. MPC given with Eq. (12) is stable, which is shown in Shetgaonkar et al. [25].

3.2.1. Inner MPC loop design

Inner MPC loop is represented in the discretized from as in Shetgaonkar et al. [25], where the corresponding continuous matrices are:

$$A = \begin{bmatrix} -\frac{R_{arm}}{L_{arm}} & 2\omega & 0 & 0 & 0 \\ -2\omega & -\frac{R_{arm}}{L_{arm}} & 0 & 0 & 0 \\ 0 & 0 & -\frac{R_{arm}}{L_{arm}} & 0 & 0 \\ 0 & 0 & 0 & -\frac{R^{ac}_{eq}}{L^{ac}_{eq}} & -\omega \\ 0 & 0 & 0 & \omega & -\frac{R^{ac}_{eq}}{L^{ac}_{eq}} \end{bmatrix}, \tag{14a}$$

$$B = \text{diag}\left\{ -\frac{1}{L_{arm}}, -\frac{1}{L_{arm}}, -\frac{1}{L_{arm}}, \frac{1}{L^{ac}_{eq}}, \frac{1}{L^{ac}_{eq}} \right\}, \tag{14b}$$

and vector $\vec{x} = [i^{\Sigma}_{d},\ i^{\Sigma}_{q},\ i^{\Sigma}_{z},\ i^{\Delta}_{d},\ i^{\Delta}_{q}]^T$ represents continuous state variables, while $\vec{u} = [v^{\Sigma}_{Md},\ v^{\Sigma}_{Mq},\ v^{\Sigma}_{Mz} - \frac{v_{dc}}{2},\ v_{Md} - v^{\Delta}_{d},\ v_{Mq} - v^{\Delta}_{q}]^T$ represents continuous system inputs.

3.2.2. Outer MPC loop design

This MPC loop is used to control DC voltage of MTDC system. This loop maintains rated DC voltage at MMC1. In order to make the inner MPC controller dynamical, linearization is avoided. Thus outer loop is added to take into account of other system variables which are indirectly derive the inner MPC loop state variables. The continuous state space representation matrices are:

$$A = \left[\frac{-1}{k_{dc} \times T_{dc}}\right], \quad B = \left[\frac{1}{k_{dc}}\right]. \tag{15}$$

The vector $\vec{x} = [v_{dc\ ref} - v_{dc}]$ represents the continuous state variable, while $\vec{u} = \left[i^{\Delta}_{d}\right]$ represents continuous system input. The k_{dc} and T_{dc} are 6.5 and 0.0035 respectively. The discretization method remains the same as for the inner MPC loop. The cost function minimizes the control signal to eliminate any deviation from rated DC link voltage. The diagram of MPC is depicted in Fig. 3.

3.3. Back-stepping control (BSC) formulation

This subsection emphasizes on the modeling of the MMC converter utilizing the BSC approach. The *Lyapunov* stability analysis is also provided to ensure the system stability.

3.3.1. State-space construction for adaptive BSC scheme

The BSC loop contains three state variables, which are the *d-q* frame grid currents i^{Δ}_{d}, i^{Δ}_{q} and the energy W_z stored in the capacitor of each MMC's sub-module. The state variables $\vec{x}$ and control variables $\vec{u}$ can be defined as follows,

$$\vec{x} = \begin{bmatrix} x_1 & x_2 & x_3 \end{bmatrix}^T = \begin{bmatrix} W_z & i^{\Delta}_{d} & i^{\Delta}_{q} \end{bmatrix}^T \tag{16a}$$

$$\vec{u} = \begin{bmatrix} u_1 & u_2 \end{bmatrix}^T = \begin{bmatrix} v^{\Delta}_{Md} & v^{\Delta}_{Mq} \end{bmatrix}^T \tag{16b}$$

where W_z provides a virtual reference for the state variable i^{Δ}_{d} and can be calculated as: $W_z = 3C(V_{dc})^2/N$, and C is the capacitance of each sub-module. Then, the MMC's dynamics can be presented as:

$$\dot{x}_1 = P_{ac} - P_{dc} = \frac{3}{2} v^{G}_{d} i^{\Delta}_{d} - P_{dc} \tag{17a}$$

$$\dot{x}_2 = \frac{1}{L^{ac}_{eq}} \left(v^{\Delta}_{Md} - R^{ac}_{eq} i^{\Delta}_{d} - \omega L^{ac}_{eq} i^{\Delta}_{q} - v^{G}_{d} \right) \tag{17b}$$

$$\dot{x}_3 = \frac{1}{L^{ac}_{eq}} \left(v^{\Delta}_{Mq} - R^{ac}_{eq} i^{\Delta}_{q} + \omega L^{ac}_{eq} i^{\Delta}_{d} - v^{G}_{q} \right) \tag{17c}$$

We define the error variables and their time derivatives as

$$\boldsymbol{e} = \begin{bmatrix} e_1 & e_2 & e_3 \end{bmatrix}^T = \begin{bmatrix} W_{\text{zef}} - W_z & e_v - i^{\Delta}_{d} & i^{\Delta}_{q,ref} - i^{\Delta}_{q} \end{bmatrix}^T \tag{18a}$$

$$\dot{\boldsymbol{e}} = \begin{bmatrix} \dot{e}_1 & \dot{e}_2 & \dot{e}_3 \end{bmatrix}^T = \begin{bmatrix} \dot{W}_{\text{zef}} - \dot{W}_z & \dot{e}_v - \dot{i}^{\Delta}_{d} & \dot{i}^{\Delta}_{q,ref} - \dot{i}^{\Delta}_{q} \end{bmatrix}^T \tag{18b}$$

where e_v is the virtual control variable from the energy controller, which corresponds to the reference value of the state variable x_2.

3.3.2. Lyapunov stability analysis

Now let us define the following quadratic *Lyapunov* function :

$$\mathrm{V}(x) = \frac{1}{2}e_1^2 + \frac{1}{2}e_2^2 + \frac{1}{2}e_3^2. \tag{19}$$

It is straightforward to conclude that $\mathrm{V}(x)$ is positive for all $e_1, e_2, e_3 \neq 0$, and is met only when the system is operating in steady-state condition $(e_1, e_2, e_3 = 0)$. According to *Lyapunov*'s direct method [11], the transient stability analysis is used to determine whether the *Lyapunov* function is decreasing along the system's trajectories. Given that the constructed *Lyapunov* function $\mathrm{V}(x)$ is differentiable everywhere, the stability of MMC operation can be ensured if the time derivative of $\mathrm{V}(x)$ is negative everywhere except in the equilibrium point, which is calculated as:

$$\dot{\mathrm{V}}(x) = e_1\dot{e}_1 + e_2\dot{e}_2 + e_3\dot{e}_3. \tag{20}$$

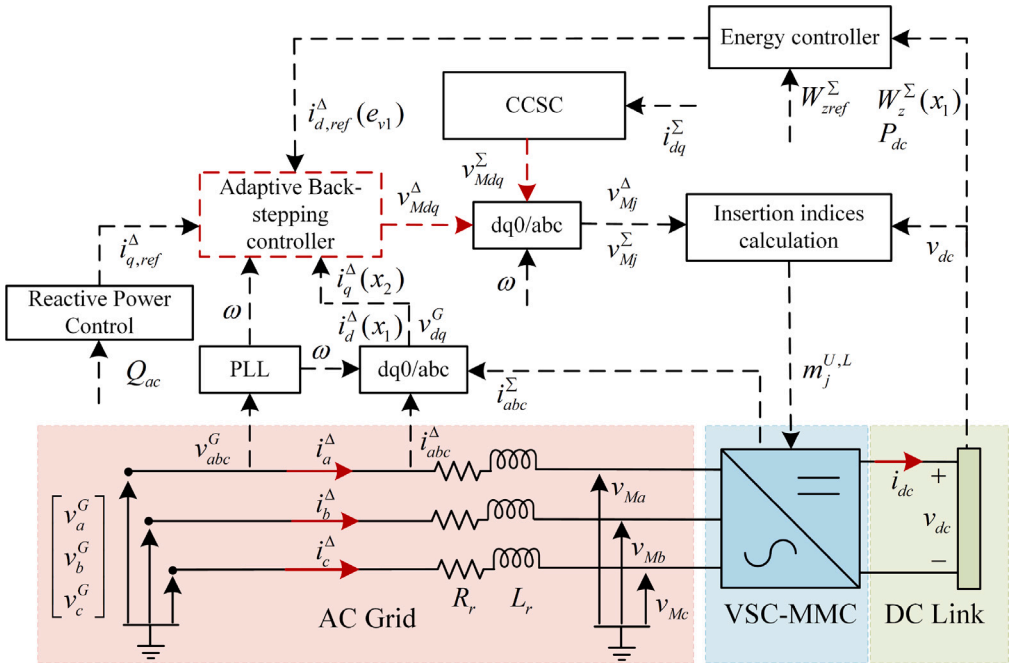

Fig. 4. Flowchart of BSC approach for MMC converter.

It is worthwhile to highlight that the energy reference W_{zef} is set as a constant value, which gives its derivative $\dot{W}_{zef}$ being 0. If the following conditions are satisfied and we guarantee that $k_1, k_2, k_3 > 0$, then $\dot{V}(x) < 0$ if:

$$e_v = 2\left(k_1 e_1 + P_{dc}\right)/3v_d^G, \tag{21a}$$

$$\dot{e}_2 - e_1 v_d^G/2 = -k_2 e_2, \tag{21b}$$

$$i_{qref}^{\Delta} - \left(v_{Mq}^{\Delta} - R_{eq}^{ac} i_q^{\Delta} + \omega L_{eq}^{ac} i_d^{\Delta} - v_q^G\right)/L_{eq}^{ac} = -k_3 e_3. \tag{21c}$$

To further eliminate the steady-state errors, additional adaptive terms θ_d and θ_q are considered [19]:

$$\theta_d = -\int k_{di} e_2 dt, \quad \theta_q = -\int k_{qi} e_3 dt, \tag{22}$$

where the k_{di} and k_{qi} are the control gains of the adaptive terms. It is noted that all adaptive terms would be zero in the steady-state. With the adaptive terms, the adaptive BSC approach ensure the system fewer overshoots and undershoots during transients. We have the final expressions of control variables v_{Md}^{Δ} and v_{Mq}^{Δ} as [27]

$$\begin{aligned} v_{Md}^{\Delta} &= L_{eq}^{ac}\left(\dot{e}_v + k_2 e_2\right) - R_{eq}^{ac} i_d^{\Delta} - L_{eq}^{ac} i_q^{\Delta}\omega - v_d^G - \int k_{di} e_2 dt, \\ v_{Mq}^{\Delta} &= \left(i_{qref}^{\Delta} + k_3 e_3\right) L_{eq}^{ac} + R_{eq}^{ac} i_q^{\Delta} - L_{eq}^{ac} i_d^{\Delta}\omega + v_q^G - \int k_{qi} e_3 dt. \end{aligned} \tag{23}$$

Up to this point, we have proved that $\dot{V}(x)$ is strictly negative everywhere, which can be expressed as: $\dot{V}(x) = -k_1 e_1^2 - k_2 e_2^2 - k_3 e_3^2$. Since the back-stepping approach exhibits more desired performance for modeling the systems with higher layers, the CCSC and outer q-axis grid current control loop adopt classical PI controllers as described in detail previously. The control gains of BSC in this work are set as: $k_1 = 0.48$, $k_2 = 0.5$, $k_3 = 0.48$, $k_{di} = 20.0$, and $k_{qi} = 20.0$, respectively. To this end, the overall BSC scheme can be described as Fig. 4.

3.4. Super-twisting sliding mode control (STSMC) formulation

The STSMC formulations for MMC are introduced. The second-order super-twisting slide mode is implemented in our work, which produces a continuous control action and preserves the accuracy and robustness features of classic SMC. Moreover, this method does not require a time derivative of the sliding surface function $\dot{S}$, which is another important feature of this method. The proposed control law for a super-twisting controller is [20,21]:

$$\dot{S}\left(i_{d,q}^{\Delta}\right) = -\alpha'\sqrt{x_{d,q}}\,\mathrm{sgn}(x_{d,q}) - \beta'\int \mathrm{sgn}(x_{d,q}),\ \alpha' > \beta' > 0, \tag{24}$$

where, $\alpha' = 1.5\sqrt{H}$ and $\beta' = 1.1H$. H is upper bound of the system disturbance. The value of H is fixed to 10. The $x_{d,q}$ are the corresponding outputs of the output current controller, defined as

$$\dot{\vec{\zeta}}_{dq}^{\Delta} = \vec{i}_{dq,ref}^{\Delta} - \vec{i}_{dq}^{\Delta}, \vec{x}_{dq}^{\Delta} = K_i^{\Delta}\vec{\zeta}_{dq} + K_p^{\Delta}\dot{\vec{\zeta}}_{dq}^{\Delta}. \tag{25}$$

It is obvious that both terms of the control input are continuous, and the chattering is attenuated. Considering the following sliding surface of degree one:

$$\begin{aligned} S(e_{vo}, t) &= \dot{e}_{vo} + \lambda e_{vo}, \\ \dot{S}(e_{vo}, t) &= \varphi_1 + \gamma v_{inv} + h(t). \end{aligned} \tag{26}$$

The final control law that must fulfill the attractivity in the presence of uncertainties and disturbances: $S(S\dot{S} \leftarrow \eta|S|, S \neq 0, \eta > 0)$, which can be calculated as:

$$\dot{S}(e_{vo}, t) = h(t) = \varphi_1 + \gamma v_{eq} \rightarrow v_{eq} = \frac{-\varphi_1}{\gamma}. \tag{27}$$

And thus the final control law can be rewritten as

$$v_{\mathrm{inv}} = v_{eq} + v_{\mathrm{un}} = -\gamma^{-1}\left(\varphi_1 + \alpha\sqrt{S}\mathrm{sgn}(S) + \beta\int \mathrm{sgn}(S)dt\right), \tag{28}$$

$\alpha > \beta > 0$.

Taking into account the MMC dynamics in Section 2, the reference voltage is calculated as

$$\vec{v}_{Mdq}^{\Delta} = -L_{eq}^{ac}\dot{\vec{S}}\left(\vec{i}_{dq}^{\Delta}\right) + R_{eq}^{ac}\vec{i}_{dq,ref}^{\Delta} + \omega L_{eq}^{ac}\mathbf{J}_2\vec{i}_{dq,ref}^{\Delta} + \vec{v}_{dq}^{G}. \tag{29}$$

4. Three-terminal MMC-HVDC power system

To investigate the interoperability of the aforementioned advanced controllers, a ±525 kV three-terminal meshed MMC-HVDC system is modeled in detail in the RTDS depicted in Fig. 5.

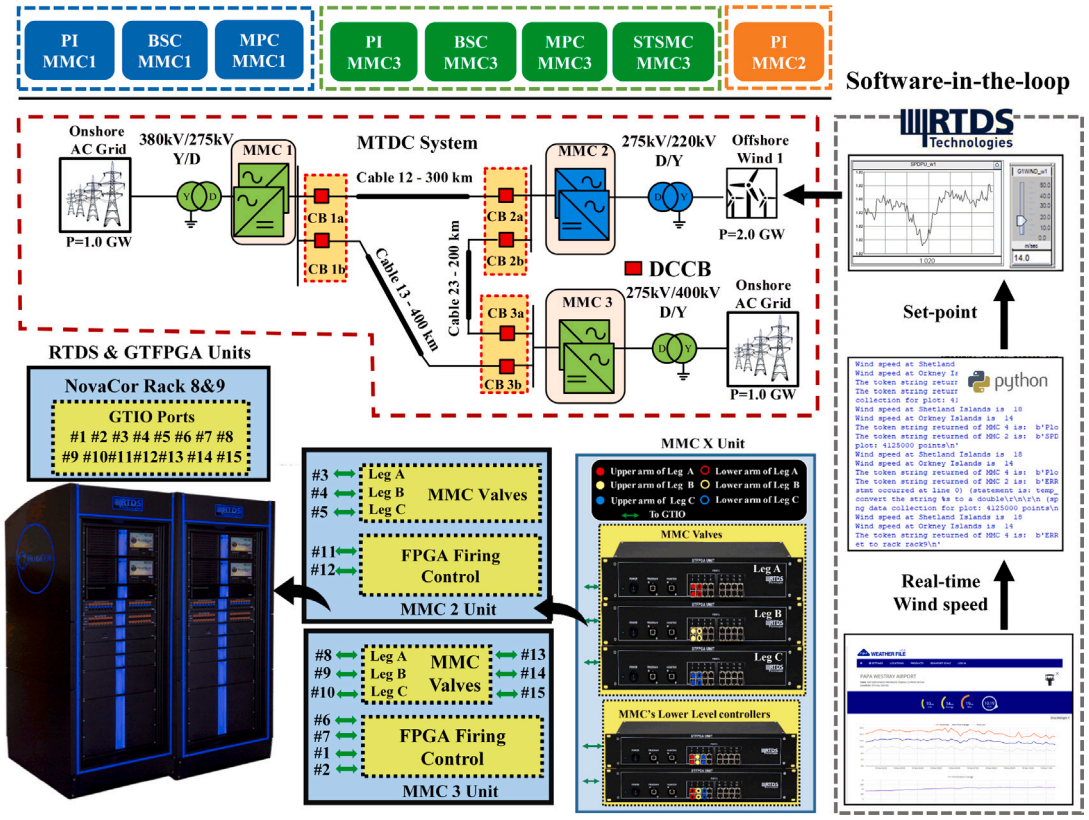

Fig. 5. Configuration of the ±525 kV three-terminal meshed MMC-HVDC system.

4.1. RTDS-based MMC modeling

In RTDS/RSCAD, MMC2 and MMC3 are using the most detailed MMC valve model: $'rtds\_vsc\_FPGA\_GM'$ [28], while the average one is adopted for MMC1. The Xilinx Virtex-7 FPGA board (GTFPGA) is used for RTDS [29] due to its high computation and parallel processing ability. Three GTFPGA units are required to represent one MMC unit. Since the capacitor voltage across all SMs must be balanced and equal, two additional GTFPGA units are required to realize the capacitor voltage balancing and firing pulse control. In this work, the odd–even sorting algorithm is utilized [30]. The number of SMs inserted per time step is calculated based on the Nearest Level Control (NLC) selection technique. Thus, five GTFPGA units are required to represent one of the detailed model $'rtds\_vsc\_FPGA\_GM'$ for MMC2 and MMC3.

Furthermore, two RTDS NovaCor racks (each with seven cores) are required to present this MTDC system from Fig. 5. It should be noted that the MTDC system, with BSC, MPC, and STSMC controllers are programmed on one RTDS rack along with the onshore and DC grid, while the wind farm is modeled on another rack. The cross-rack communication is performed by a global bus hub and an IRC switch. The GTFPGA units are connected to the GTIO port of RTDS NovaCor racks, and the signal exchanges are done through two full-duplex fiber optic cables using standard high-speed Aurora protocol.

Table 2 lists the system ratings and selected parameters.

4.2. XLPE cable and wind farms

A suitable cable ratings are required to link the offshore wind farms to the onshore grid system. The submarine XLPE cable is used and modeled within the RTDS environment using frequency dependent model (phase domain). The parameters for cables are taken from Wachal et al. [23]. The length of cable12, cable23, and cable13 are 300 km, 200 km, and 400 km, respectively. The MMC1 and MMC3 connect the strong onshore AC grid with 1 GW rated power. The offshore wind farms connect the DC grid through MMC2, built in small time steps with eight parallel connected type 4 wind turbines. An interface transformer connects the small time step model to the large time step model. Furthermore, the active power can be scaled to the desired level. The software-in-the-loop (SIL) is used to extract the real-time wind speeds from the web by the *Selenium* tool, as illustrated in Fig. 5. The online wind data are communicated through TCP/IP connection to RSCAD, the communication delay is 100 ms, and the data is updated every 2 s. The wind gust data is measured near the Orkney Islands (58.9809° N, 2.9605° W) and Shetland Islands (60.5297° N, 1.2659° W), which is adopted from [31].

Table 2
System parameters.

Item	Converters		
	MMC1	MMC2	MMC3
Rated Active Power	1000 MW	2000 MW	1000 MW
Control Mode	V_{dc}/V_{ac}	P_{ac}/Q_{ac}	v_{ac}/f
DC Link Voltage	±525 kV		
SMs Number Per Arm	200		
Arm Capacitance	15000 μF		
Arm Inductance	39.7 mH		
DC Inductance	20 mH		
AC Converter Voltage	275 kV		
Transformer Inductance	0.18 pu		
AC Grid Voltage	380 kV	220 kV	400 kV

4.3. DC circuit breaker settlings

The power-electronic equipment are vulnerable to DC faults, and it is crucial to implement the DC protections and DC Circuit Breakers

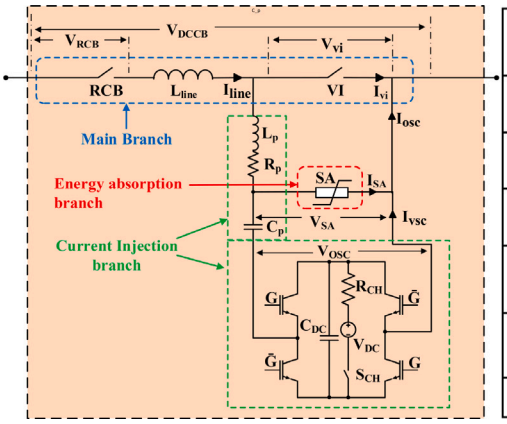

Items	Symbol	320kV VARC	525kV VARC
Oscillation Inductor	L_p	300 μH	492.18 μH
Oscillation Resistor	R_p	0.5 Ω	0.82 Ω
Oscillation Capacitor	C_p	0.66 μH	0.40 μH
SA Rated voltage	-	320/ 480kV	525/ 787.5kV
Initial voltage across C_p	$V_{in}C_p$	24kV	39.37kV
Line inductor	L_{line}	80 mH	80 mH

Fig. 6. Graphical representation of VARC CB and scaled 525 kV parameters.

Table 3
SIEMENS TWP thresholds.

Item	Δset_1 (kV/ms)	Δset_2 (kV)	Δset_3 (kA/ms)	Δset_4 (kA)
Cable12	254.29	478.8	2.712	3.67
Cable13	278.74	316.2	5.76	7.26
Cable23	138.01	234.02	4.71	6.63

(DC CBs) to detect the faults within 2 ms [32] and interrupt the fault currents nearly instantly [33,34]. Our testing system adopts the non-unit SIEMENS traveling wave protection (TWP), which utilizes the current derivative (di/dt) and voltage derivative (du/dt) of traveling waves sampled at the relay unit. The detailed SIEMENS TWP protection criterion is:

$$\begin{cases} \dfrac{du}{dt} > \Delta set_1, \\ \Delta u > \Delta set_2, \end{cases} \quad \begin{cases} \dfrac{di}{dt} > \Delta set_3 \text{ (Rectifier side)}, \\ \Delta i > \Delta set_4 \text{ (Inverter side)}, \end{cases} \tag{30}$$

where $\Delta set_i (i = 1, 2, 3, 4)$ are the thresholds for fault detection. Following the design procedures illustrated in Zhang et al. [35], the thresholds of SIEMENS TWP for each cable are listed in Table 3. When all the criteria are satisfied, the protection trips the corresponding DCCB to interrupt the fault currents.

Due to the fast interruption speed, the VSC-assisted resonant current (VARC) DCCB are selected and implemented at each cable terminal. Detailed model structure, operating principle, and experimental testing of VARC CB can be found in Liu et al. [36]. It is noted that the authors of Liu et al. [36] use four series 80 kV VARC modules achieving the ±320 kV voltage level, which introduces an extra computational burden. The main goal of this work is to investigate the interoperability between the controllers during system transients. Thus, we have aggregated the series 80 kV VARC modules into ±525 kV voltage levels for simplification. It is worth mentioning that a small solution-time step (1 or 2 μs) is needed in simulation to generate the high-frequency oscillating current. The representation of the scaled VARC DCCB and the specific parameters can be found in Fig. 6.

4.4. MMC controller allocations

The control hierarchy for the high power converter can be classified into three regions as depicted in Fig. 7. Region 1 (pink colored area in Fig. 7), represents the converter level control compresses of capacitor voltage balancing, circulating current suppression and IGBT switching pluses. Typically this region operates within tens or hundreds of microseconds. Region 2 (light blue colored area in Fig. 7), provides the reference signals for the control loops from region 1 based on the dispatch control signal provided by region 3 (light green colored area in Fig. 7). Region 2 is also known as station level control and has a response time of a few hundred milliseconds. In this paper, we focus on Region 2 for which are different controllers implemented.

Table 4
Different control allocation scenarios for MMC1 and MMC3.

Uniformed		Mixed	
Scenario	MMC1-MMC3	Scenario	MMC1-MMC3
S1	PI(V_{dc}/V_{ac})-PI(P_{ac}/Q_{ac})	S5	PI(V_{dc}/V_{ac})-BSC
S2	MPC-MPC	S6	MPC-STSMC
S3	BSC-BSC	S7	MPC-BSC
S4	PI(V_{dc}/V_{ac})-STSMC	S8	BSC-STSMC

In the studied system from Fig. 5, all MMCs can be controlled via PI controllers, as explained in Section 3. Furthermore, the MPC method is implemented in MMC1 and MMC3. The BSC method is implemented in MMC1 and MMC3, and the STSMC is implemented in MMC3. To investigate the IOP and interactions of different controllers for MMC1 and MCM3, the following eight scenarios (twelve possible in total) are defined for simulation studies as Table 4. The scenarios 'PI-MPC', 'MPC-PI', 'BSC-MPC', 'BSC-PI' may result in unstable oscillatory behaviors, they are omitted due to the concern of lengthy paper and their insufficient interoperability.

5. Simulation studies

In this section, an in-depth analysis is carried out to investigate the interoperability of various controllers. Hence, simulations are performed based on the three-terminal HVDC-based power system using HIL RTDS experiments. We demonstrate that non-linear controllers achieve the faster transitions with minimal DC voltage and active power variations, and current peak values during the system transients. Thus, we define the following indicators to assess the controller performance:

- t_r: Rise time for the response signal to increase/decrease from the initial value to 90% of expected value.
- t_s: Settling time for the response signal to reach and stay within a range of 3% of expected value (error band).
- P_{var}: Maximum variation of active power during transient response.
- V_{var}: Maximum variation of DC voltage during transient response.
- i_P: Maximum peak current during transient response.

The transient cases investigated are:

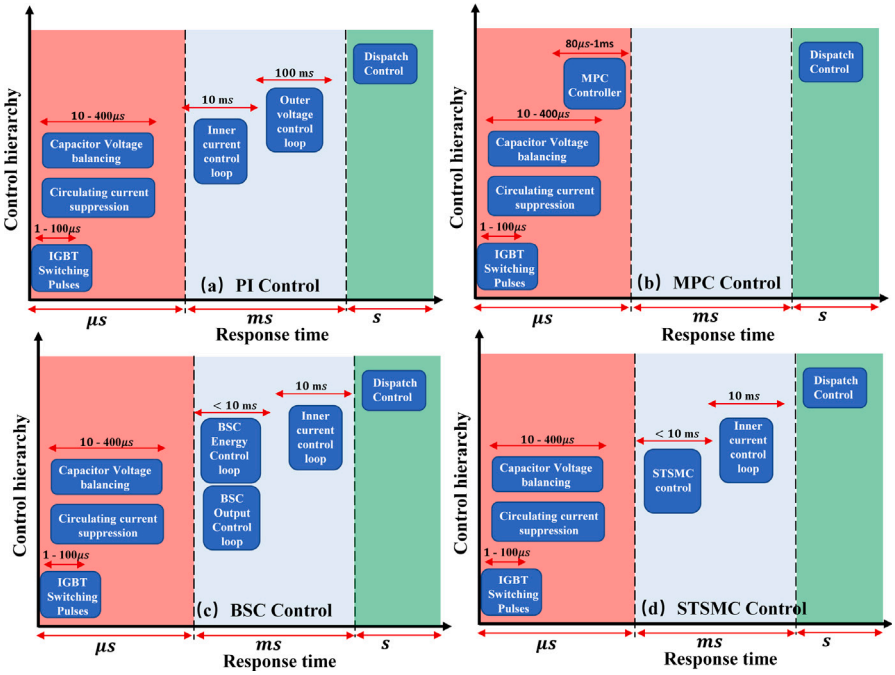

Fig. 7. MMC control hierarchy: (a) PI hierarchy. (b) MPC hierarchy. (c) BSC hierarchy. (d) STSMC hierarchy.

- Case I: Step change of MMC3's active power from 0 p.u. to 0.5 p.u. at $t_0 = 0.1$ s (Event1) and increase to 1.0 p.u. at $t_1 = 1.1$ s (Event2).
- Case II: Temporary positive-pole to ground (PTG) fault occurs at cable12 outlet at $t_0 = 0.1$ s (Event1) and VARC DCCB re-closes at $t_1 = 1.1$ s (Event2).
- Case III: Step change of wind farms output power from 630 MW to 750 MW at $t_0 = 0.5$ s (Event1) and increase to 1000 MW $t_1 = 5.5$ s (Event2).
- Case IV: Temporary phase A grounding fault occurs at MMC1 AC gird at $t_0 = 0.1$ s (Event1), fault resistance is 1.0 Ω.
- Case V: MMC1's controller switching from PI to BSC at $t_0 = 0.1$ s (Event1), BSC to MPC at $t_1 = 1.1$ s (Event2), and MMC3 controller switching from PI to BSC at $t_0 = 0.1$ s (Event1), BSC to STSMC at $t_1 = 1.1$ s (Event2), STSMC to MPC at $t_2 = 2.1$ s (Event3).

5.1. Case I: Step change of active power

The rating active power of MMC3 is set to 1000 MW (1 p.u.). MMC1 maintains the DC grid voltage and acts like a slack bus in the DC grid, MMC2 supplies active power from wind farms, while MMC3 regulators the active power flow. Before the disturbance, the reference active power $P_{ac,ref}$ of MMC3 is set as 0 p.u., the power produced by the wind farms through MMC2 is all absorbed by MMC1. At time instance $t_0 = 0.1$ s, there is a step change in the $P_{ac,ref}$ of MMC3 rising from 0 p.u. to 0.5 p.u. (Event1). Different controller combinations 4 present different behaviors to this system transient. Fig. 8 provides the simulation results of the active power exchanges between MMC1 and MMC3.

According to Fig. 8(a), the waveform of P_{MMC3} is smooth and does not oscillate in the case of scenario PI-PI (S1). However, the speed of response and settling is significantly slower than the other scenarios due to the higher time constant of PI control in the outer loop. In contrast to S1, the scenario MPC-MPC (S2) has the optimal performance of the rising and settling time and minimal power variation (almost none). In the case of scenario BSC-BSC (S3), the converge time is shorter than in scenario S1, and a small degree of variation can be found. This is because the reference signal of i_d^A of BSC comes from the upper-level energy controller, which is designed to reflect the variations of DC voltage. Thus, the tracking ability of active power step-changing is relatively weak. When the MMC3 is controlled via STSMC (S4), a large degree of variation is observed, since the STSMC is turned to provide faster response as consequence creates overshoot. A similar result is also found in S8. For other controller allocations, the settling and rise time are reduced compared with scenario PI-PI (S1), and the power variations are also smaller than in scenarios S4, S6, and S8. Fig. 8(b) presents the waveform of MMC1 active power, the scenario PI-PI (S1) presents an even longer rise and settling time than that of MMC3. The MMC 3 absorbs the power from the DC grid. However, the response of MMC 1's outer control is slower (in case of S1). The energy is taken from the DC voltage, which creates a drop in DC voltage. Thus, the tracking ability of MMC1 is not robust enough against active power step change. In the case of scenarios S2, S6, and S7, the active power P_{MMC1} is converging with an oscillating frequency (from 9.21 Hz to 9.66 Hz) as a result of interaction between inner and outer control loops. Other scenarios are similar to that of MMC3. The transient process of Event2 is similar to that found in Event1.

The dynamics of active power also leads to variations of DC voltage. Fig. 9 provides the simulation for DC voltages V_{dc3} and V_{dc1}. The maximum percentage variation in the DC voltage varies with different controller allocations. It is obvious that in the case of scenario PI-PI (S1), the voltage V_{dc3} and V_{dc1} have the largest voltage variations which exceed the error band, and the settling time both at MMC3 and MMC1 is longer than that of other scenarios by reason of the high time constant settling in MMC3 PI outer loop. In contrast, small fluctuations are observed in some control scenarios, e.g., S2, S6 and S7, but can be restricted within a 3% standard margin. For other controller allocations, e,g., S3, S5, and S8, the waveforms of V_{dc3} and V_{dc1} are smooth and without any oscillations. Overall, these scenarios with advanced controllers present a more desirable performance than that of classical controller allocation S1.

Table 5 provides the detailed summary statistics obtained from the preliminary analysis of case I. It is apparent that the rise time t_r of S1 in case of P_{MMC3} and P_{MMC1} are much longer than in other scenarios

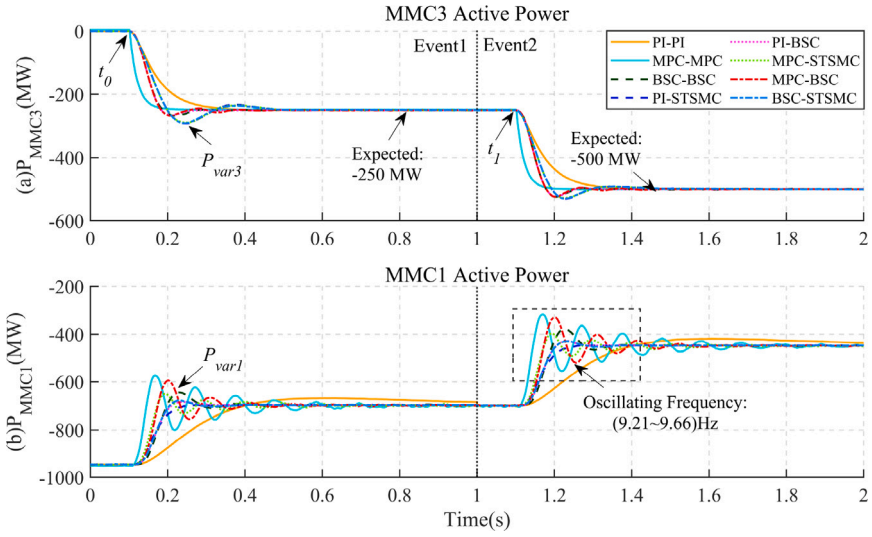

Fig. 8. Simulation of case I: (a) MMC3 active power. (b) MMC1 active power.

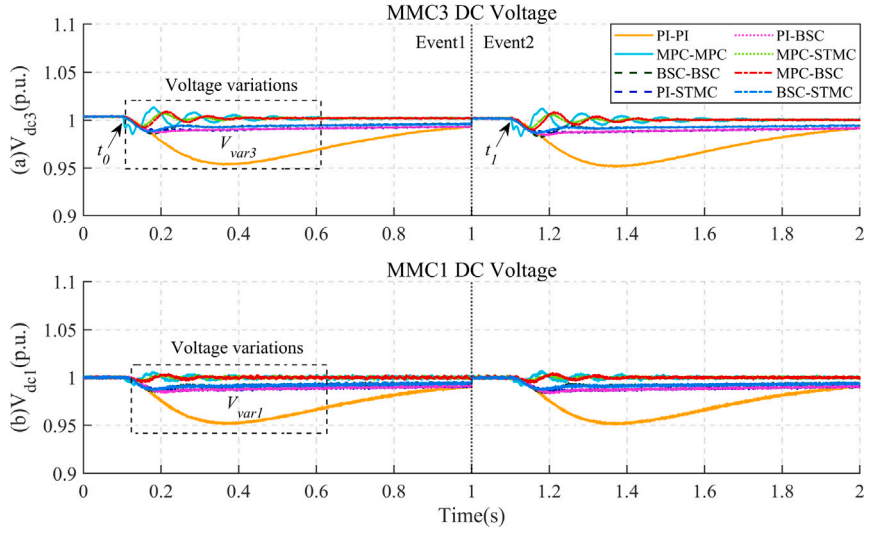

Fig. 9. Simulation of case I: (a) MMC3 DC voltage. (b) MMC1 DC voltage.

by cause of MMC1's DC voltage control settling. But except for S2, the variation of P_{MMC3} in S1 is much smaller than in all other scenarios due to its smooth process. While for some scenarios, e.g., S4, S6, and S8, they are designed with a fast-tracking capability, which improves the rise time but in the meantime, it causes significant fluctuations due to the excessive damping during transients. This further prolongs the settling time which is even longer than S1. This phenomenon also applies and is even more obvious for the in P_{MMC1} of MMC1. For the DC voltage variations, the S1 has the largest variations, which reach 4.88% and 4.92%, respectively. Other scenarios have optimal performance in maintaining the DC voltage, the fluctuations are restricted within the margin of 2%, among them the S6 obtains the optimal behavior with 0.85% and 0.49% variations at each side. The scenario S4 (PI-STSMC) is suggested as the optimal choice to regulator the active power, since it has minimal power and voltage variations, and fastest rise and settling time, S5 (PI-BSC) and S8 (BSC-STSMC) can be set as the back-up scenarios.

Table 5
Simulation data for case I.

Item	Event1							
	P_{MMC3}			P_{MMC1}			V_{dc3}	V_{dc1}
	t_r (s)	t_s (s)	P_{var3} (%)	t_r (s)	t_s (s)	P_{var1} (%)	V_{var3} (%)	V_{var1} (%)
S1	0.154	0.220	0.053	0.192	0.766	6.525	4.88	4.92
S2	0.050	0.079	0.012	0.039	0.381	29.191	1.70	0.86
S3	0.073	0.153	4.823	0.081	0.168	15.50	1.79	1.64
S4	0.089	0.339	6.070	0.083	0.112	0.49	1.36	1.49
S5	0.072	0.138	4.710	0.081	0.097	4.578	1.62	1.68
S6	0.088	0.347	5.529	0.061	0.201	11.472	0.85	0.49
S7	0.072	0.1323	4.768	0.065	0.229	26.353	1.06	0.67
S8	0.089	0.338	6.009	0.080	0.136	4.077	1.40	1.32

5.2. Case II: DC fault and DCCB re-closing

Fig. 10 provides diagrams which represent successful fault interruption in cable12. The term iline12 used in Fig. 10(a) refers to the

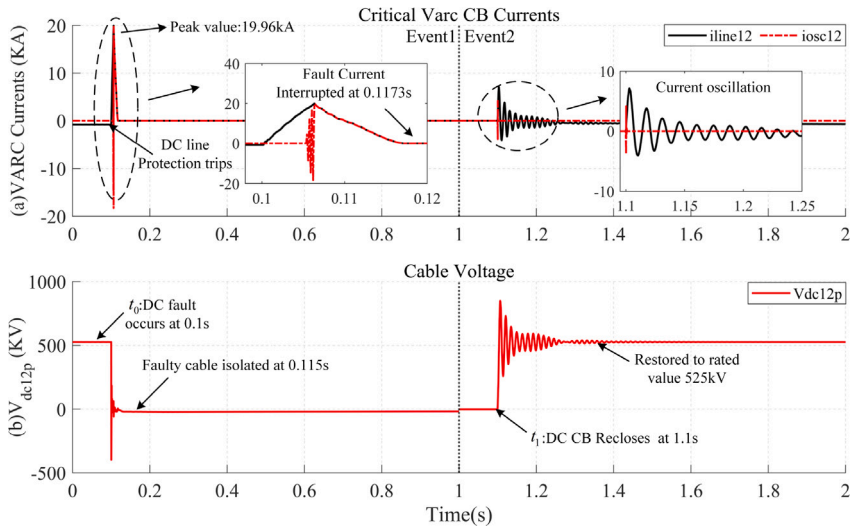

Fig. 10. Simulation of case II: (a) VARC currents. (b) Cable12 voltage.

line current, the term iosc12 is defined as high-frequency oscillating current of the VSC-branch of VARC DCCB to create the zero-crossing. Since the PTG fault is applied at $t_0 = 0.1$ s at the cable12 outlet, the SIEMENS TWP immediately detects the fault and trips the VARC DCCB installed at the positive pole of cable12 (near MMC1), while the DCCB near MMC2 is tripped with a time-delay due to the fault traveling wave propagation across the cable12.

As can be seen in Fig. 10(a), the current iline12 continues to increase until iosc12 reaches the same amplitude (reversal direction) and is communicated to the main breaker. The peak value of fault current, in this case, is 19.96 kA. The fault is successfully interrupted at 0.1173 s. Meanwhile, the fault pole voltage is also cleared at 0.115 s as found in Fig. 10(b). We assume that the fault is a temporary fault, the VARC DCCB is initialed at $t_1 = 1.1$ s to reconnect the cable12. It is revealed that both cable current and pole voltage can be restored to a steady value after oscillations, which will propagate into other parts of the MTDC system. Thus, the optimal coordination between MMC controllers will be crucial in maintaining the system's stability.

Fig. 11 provides the performance of MMC1 and MMC3 (MMC2 is minimally affected) with different scenarios during the two events described in case II. Initially, the system operates at rated values. Since the DC fault is one of the most serious faults in the MTDC system, it is seen in Fig. 11(a) that the voltage V_{dc1} of MMC1 in all scenarios suffers severe oscillations. However, it is worth mentioning that all the scenarios can restore the DC voltage quickly except for S1 due to the low response ability of DC voltage control. Similar results are also observable when the VARC DCCB is re-closed at $t_1 = 1.1$ s. The MMC1's output current i_{MMC1} is depicted in Fig. 11(b). At the initial fault stage, the i_{MMC1} also increases rapidly. The majority of fault currents are the discharging currents of MMC arm capacitors. Different scenarios demonstrate different fault current suppression capabilities, the fault peak current ranges from 14.36 kA to 16.53 kA and the current will be restored to nominal value when DCCB clears the fault. When the DCCB is re-closed at $t_1 = 1.1$ s (Event2), the topology of the system is modified, and the power flow is reallocated, which can be learned from Fig. 11(b) and (c). Thus, the current i_{MMC1} will be restored to the new steady-state value with an oscillating frequency 80.80 Hz. This newly added cable introduces a time delay due to the inductive nature of the cable. As a result, time response of all scenarios varies within a range of a few milliseconds, the settling time t_s, in this case, is around 120 ms. The peak value is restricted to the range from 5.10 kA to 6.29 kA. As can be seen in Fig. 11(c), the MMC3's active power P_{MMC3} is also highly affected at fault initial and post-fault stage.

The maximum variations and settling times vary in different scenarios. Detailed summary obtained from the case II can be found in Table 6. In Event1, the voltage variation V_{var1} for all scenarios exceeded 30%. Among them, S3 and S8 have the largest value of 39.72% and 39.80%, respectively, and V_{var1} with S4 and S5 are relatively small at 30.16% and 30.14%, respectively. However, the S4 and S5 present large power variations P_{var3} in Event2. In contrast, the current peak value i_{P1} of S3 and S8 are suppressed to the minimum values of 14.3679 kA and 14.4106 kA, respectively. While the S4 and S5 present the lowest current suppression capability. This is due to higher drop in the DC voltage at MMC 1 as seen in Table 6. What can be seen in this table of Event2 is that the combination of the advanced and classical controller does not provide any improved performance compared to S1. All the scenarios fail to maintain the DC voltage V_{var1} of MMC1 when the DCCB is re-closed, as they all drop sharply by 19%. The peak current i_{P1} of MMC1 is also much larger than the steady-state value, although there is a degree of variation between different scenarios. For the active power of P_{MMC3}, the S1 and S2 present relatively minimal variations, which are 2.2135% and 1.3563%, respectively. The optimal scenario selection against DC fault depend on the control priority. In the fault interruption stage (Event1). If the aim is to suppress the fault current, S3 (BSC-BSC) can be selected as it has the minimal peak value of i_{P1} as 14.3679 kA, and S8 (BSC-STSMC) can be set as the back-up scenario. If the aim is to maintain the DC voltae V_{dc1}, then S5 (PI-BSC) is the optimal settling as it has the minimal variation $V_{var1} = 30.14\%$. S4 (PI-STSMC) can be set as the back up scenario. S2 (MPC-MPC) is the first choice if the aim is to maintain the active power flow of MMC3 side, and S1 (PI-PI) can be the back-up choice. In the DCCB re-closing stage, S2 is the optimal settling as it has desired performance both in suppressing the oscillating current and maintaining the active power flow at MMC3.

Table 6
Simulation data for case II.

Item	Event1			Event2		
	LV_{dc1}	i_{MMC1}	P_{MMC3}	V_{dc1}	i_{MMC1}	P_{MMC3}
	V_{var3} (%)	Li_{P1} (kA)	P_{var3} (%)	V_{var3} (%)	i_{P1} (kA)	P_{var3} (%)
S1	36.51	15.0043	1.642	19.25	−6.2930	2.214
S2	35.25	15.1715	0.799	19.21	−5.1433	1.356
S3	39.72	14.3679	3.088	19.51	−6.1568	5.287
S4	30.16	16.5320	5.059	19.03	−5.2855	7.615
S5	30.14	16.5279	4.572	19.08	−5.2514	6.574
S6	35.2	15.1746	4.076	19.29	−5.1863	6.614
S7	35.14	15.1803	4.676	19.39	−5.1015	5.427
S8	39.80	14.4106	4.009	19.60	−6.2426	6.453

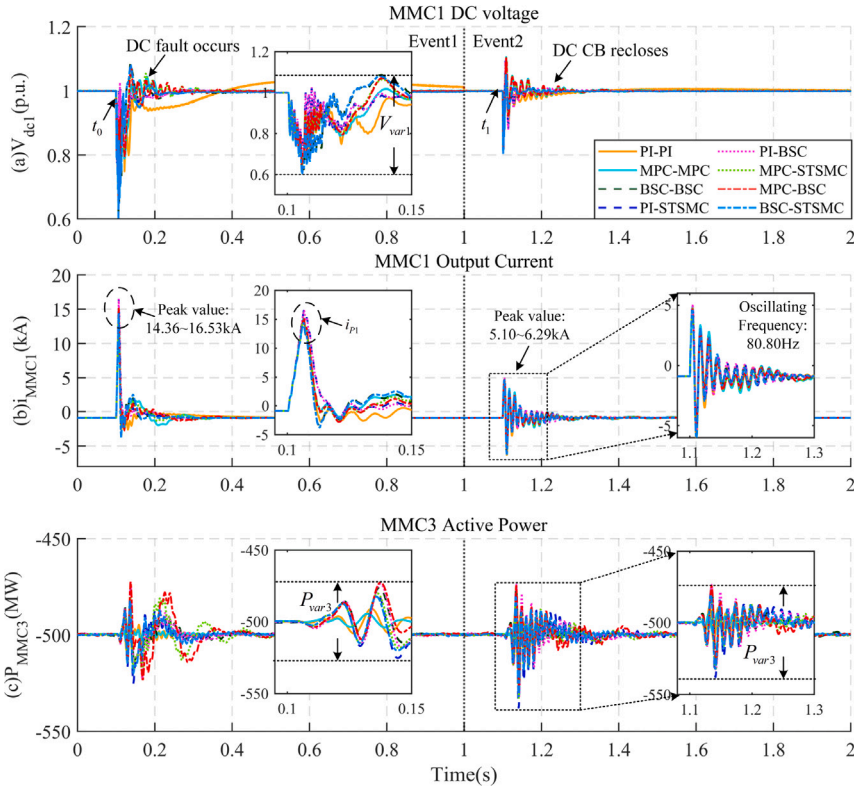

Fig. 11. Simulation of case II: (a) MMC1 DC voltage. (b) MMC1 output current. (c) MMC3 active power.

5.3. Case III: Wind-speed change

The active power P_{MMC2} depends on the wind speed of wind turbines. Fig. 12 provides the waveforms of active power in different scenarios for case III. Initially, all output active powers remain steady. Assuming that the wind speed is changed at the time instance $t_0 = 0.5$ s, the active power generated by wind farm P_{MMC2} starts to increase. Since the MMC2 is independently controlled via the grid-forming PI controller, the transient of P_{MMC2} is not affected by the controller allocations of MMC1 and MMC2. According to Fig. 12(a), the P_{MMC2} increase smoothly to the preset new condition 750 MW, the rise time t_r and settling time t_s are 0.51 s and 0.74 s, respectively. The overshoots or undershoots of P_{MMC2} are not observed during this transient. Similar results are also found in Event2. As for the P_{MMC1} presented in Fig. 12(b), all the scenarios with advanced controllers have optimal performance except for the scenario PI-PI (S1). S1 have the longest settling time t_s and the power variation is also observable. This longer power variation is created as the outer control loop of MMC1 and it is associated with DC voltage variations. It is not sensitive to the power flow changing of DC grid. While for the P_{MMC3} depicted in Fig. 12(c), it is seen that P_{MMC3} remain the steady value, only minor fluctuations can be seen. The constant power flow in MMC3 is due to the nature of control mode i.e P/Q control. However, the small perturbation arises caused by the variation of DC grid voltage around operating point.

Detailed data of rise and settling time of active power P_{MMC1} are listed in Table 7. What stands out in this table is that the settling time t_s of scenario S1 for events 1 and 2 are 1.0376 s and 0.9147 s, respectively, which are the longest. The results are aligned with preliminary analysis and also demonstrate the superior performance of these advanced controllers in terms of tracking signal. It is concluded that S2 (MPC-MPC) is the optimal choice for regulating the active power flow, since it requires the minimal settling time to the achieve the pre-set value, S3 (BSC-BSC) and S4 (PI-STSMC) can be the back-up scenarios. Other scenarios are also have desirable performance except for S1.

Table 7
Simulation data for case III.

Item	Event1		Event2	
	P_{MMC1}		P_{MMC1}	
	t_r (s)	t_s (s)	t_r (s)	t_s (s)
S1	0.3929	1.0376	0.4975	0.9147
S2	0.3600	0.5665	0.5731	0.5726
S3	0.3643	0.5856	0.5734	0.5730
S4	0.3724	0.5793	0.5878	0.5873
S5	0.3691	0.5820	0.5949	0.5944
S6	0.3587	0.6493	0.5713	0.5996
S7	0.3466	0.6400	0.5938	0.6122
S8	0.3620	0.5928	0.5896	0.5891

5.4. Case IV: AC fault study

The single phase to ground fault is the most common fault in the AC grid. Fig. 13 revels the effect of case IV for MMC1's outputs. The initial conditions are the same as in the previous subsections. After the fault occurs at $t_0 = 0.1$ s, the oscillations of MMC outputs are perceptible in all scenarios. Recall that MMC1 adopts the V_{dc}/V_{ac} control mode. An AC gird fault can be considered as a sudden disturbance signal imposed to v_{ac}. Therefore, the $i^{\Sigma}_{q,ref}$ of the outer control loop will change abruptly, which leads to the sudden change of v^{Σ}_{Mq} of the inner loop. Besides, the v^{G}_{d} and v^{G}_{q} and the frequency as the output of PLL are also affected by the fault. As a result, the inputs of the capacitor voltage balancing controller and firing control of MMC1 will be disturbed. Eventually, the DC side outputs of MMC1 are fluctuating.

More precisely, the MMC1's DC voltage is depicted in Fig. 13(a), the impact of AC fault on V_{dc1} is much smaller than that of a DC fault in any scenario, as illustrated in Fig. 11(a). This is because the variation of V_{dc1} is mainly affected by the voltage variation on the DC side. Fig. 13(b) depicts waveform of the MMC1's output current i_{MMC1}. Since i_{MMC1} represents sum of the upper and lower arm currents of MMC1, the

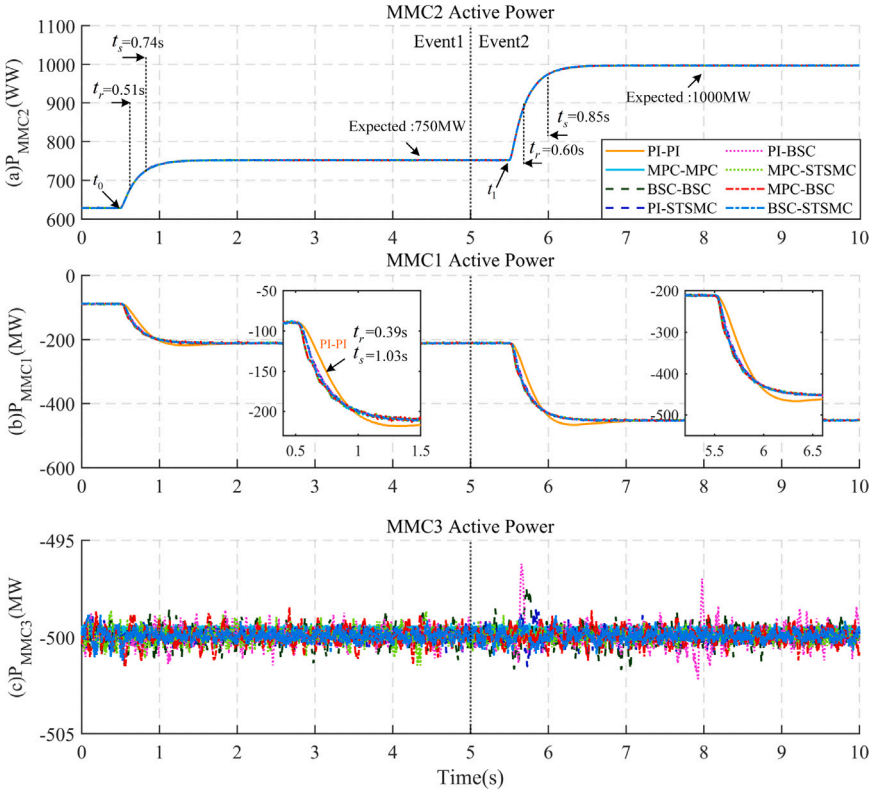

Fig. 12. Simulation of case III: (a) MMC2 active power. (b) MMC1 active power. (c) MMC3 active power.

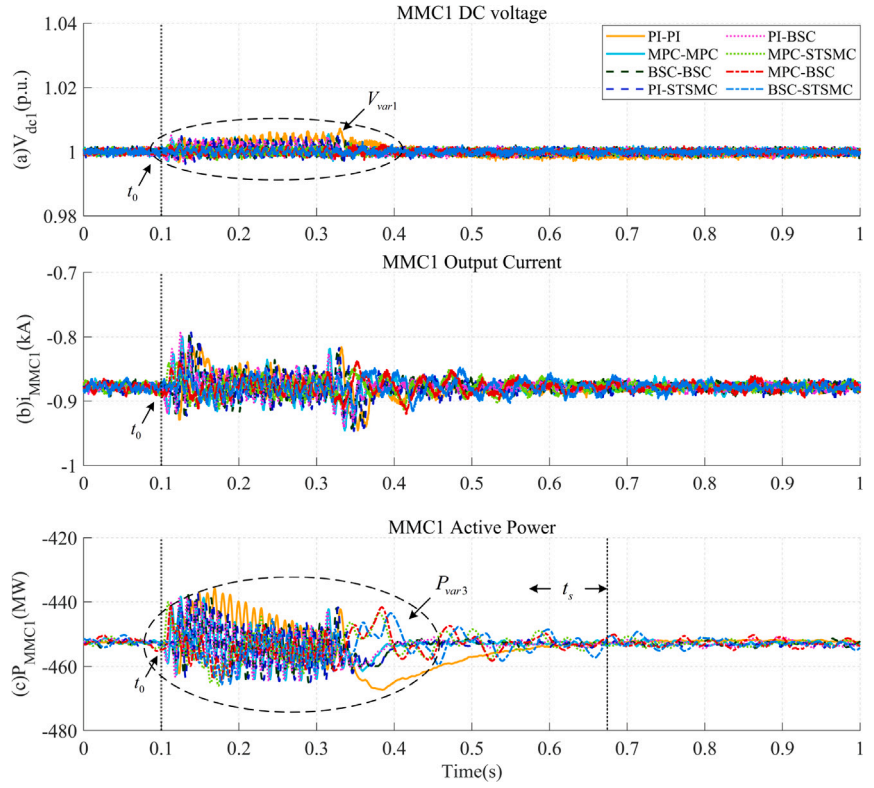

Fig. 13. Simulation of case IV: (a) MMC1 DC Voltage. (b) MMC1 output current. (c) MMC1 active power.

Table 8
Simulation data for case IV.

Item	Event1				
	V_{dc1}	i_{MMC1}		P_{MMC1}	
	V_{var1} (%)	i_{P1} (kA)	t_s (s)	P_{var1} (%)	t_s (s)
S1	0.0072	0.9456	0.2914	3.4047	0.2968
S2	0.0055	0.9458	0.1606	2.7570	–
S3	0.0048	0.9469	0.1719	2.9288	–
S4	0.0053	0.9466	0.4679	2.8643	–
S5	0.0051	0.9410	0.1610	2.8217	–
S6	0.0026	0.9130	0.3363	3.1214	0.0746
S7	0.0026	0.9210	0.3353	2.7503	–
S8	0.0030	0.9164	0.5500	3.0438	0.0785

AC fault will cause the sudden change of the grid current $i^{\Delta}_{a,b,c}$ and disrupt the balance of MMC1's arm currents. As a result, the circulating currents $i^{\Sigma}_{a,b,c}$ will increase rapidly (almost zero in the steady-state) until the disappearance of the AC fault. Then, the i_{MMC1} gradually restores to the steady-state value. The oscillations of i_{MMC1} caused by AC fault are much smaller than that of DC fault as depicted in Fig. 11(b), since V_{dc1} in this case remains stable, the SMs capacitors are not discharged after fault. Similar results of P_{MMC1} can be found in Fig. 13(c) as it is the product of V_{dc1} and i_{MMC1}. In addition, it is worth mentioning that the second-order harmonics will appear in the DC components, since the PLL cannot isolate the asymmetrical positive and negative sequence components contained in the AC grid voltages and currents by the single phase to ground fault.

The variations and settling times of case IV are summarized in Table 8. It is visible that all the scenarios present desirable performance in maintaining the DC voltage V_{dc1}, the largest variation of V_{var1} is only 0.0072% (S1). For the output current i_{MMC1}, the amplitude in steady-state is 0.887 kA. After fault, the transient peak value i_{P1} is restricted to 0.9469 kA (S3). The oscillations of fault current in i_{MMC1} are suppressed to steady-state value within 0.55 s for any scenario, which confirms the indispensability of the CCSC loop of each controller. For the active power P_{MMC1}, it is seen that it exceeds the $\pm 3\%$ error band only in the scenarios S1, S6 and S8. The largest variation of P_{var1} is 3.4047% and it is settled after 0.2968 s, other two scenarios stabilize the P_{MMC1} after 0.0746 s and 0.0785 s, respectively. The statistics fully demonstrate the robustness of each scenario against the AC grid fault. The system stability is guaranteed. It is concluded that the S2 (MPC-MPC) and S5 (PI-BSC) are the optimal scenarios against AC grid fault, since they have the minimal settling time to restore the system to the original steady-state. Other scenarios present slower settling times or larger active power variations at MMC1.

5.5. Case V: Switching between different controllers

Fig. 14 illustrates the transition effect between different controllers of MMC1. PI control is the initial control method as it is the most commonly utilized method in practical projects. The change in MMC1 control from PI to BSC is applied at the time instance $t_0 = 0.1$ s. It is seen in Fig. 14, that the DC outputs of MMC1 and MMC3 remain steady, and only a small variation of P_{var1} (2.16%) is observed in P_{MMC1}, which reveals that switching between PI and BSC can be realized smoothly and without bringing extra oscillations to the system. In the case of the controller switching from BSC to MPC (Event2) at $t_1 = 1.1$ s, there is an oscillation of 56.49 Hz with an overshoot of 4.63% in DC link voltage V_{dc1}. This oscillation occurs due to the mismatch between the output of the inner current controllers. During the operation of BSC, the MPC output is saturated. Upon the transition, the saturated value of MPC control is applied to the MMC1. As a result, MMC1 injects less power into the DC grid, which further increases the DC link voltage V_{dc1}. Later, the outer DC voltage controller regulates this voltage mismatch and restores the system. Furthermore, Fig. 15 illustrates the effect of transitions between different controllers implemented in MMC3. The switching from PI to BSC is applied at $t_0 = 0.1$ s, and all the DC voltages of MMC1 and MMC3 remain steady. When the control switches form BSC to STSMC at $t_1 = 1.1$ s, small fluctuations are visible at V_{dc1} and V_{dc3}, which reach to 1.21% and 0.54%, respectively. This is caused by the saturation of the control signal in opposite polarity, which leads to power overshoots and further creates DC link voltage overshoots. Similarly, the output currents i_{MMC1} and i_{MMC3} are also affected, with peak values of −1.0319 kA and −1.027 kA, respectively. Since extra power is taken from the DC grid at MMC2, a power mismatch of STSMC controller affects the P_{MMC3}, and the variation P_{var3} reaches 60.0%. When the controller switches from STSMC to MPC at $t_2 = 2.1$ s (Event2), it is found in Fig. 15(a) that DC voltage V_{dc3} is oscillating with the 136.61 Hz due to the faster action of MPC and slower response of STSMC, the oscillations are restored to steady-state at 2.273 s, the maximum variation of V_{var3} is restricted to 2.05%. Since the control action takes place at MMC3 with limited power variation, the V_{dc1} remains constant. The oscillating behaviors of currents i_{MMC1} and i_{MMC3} are similar to that of DC voltages, the peak values during this transient reach −1.30 kA and −1.175 kA, respectively. While for the active power presented at Fig. 15(c), small variations are found in P_{MMC1} and P_{MMC3}, the P_{var3} reaches to 10.1%, which is larger than P_{var1} (6.24%) due to higher voltage oscillations.

The results of this investigation show that all classical and advanced controllers implemented in MMC1 and MMC3 can switch between each other. Although there are some undesired fluctuations on the DC side in some scenarios, most are within the acceptable 3% error band. More prominent disturbances are quickly adjusted to steady-state values by the controller and will not cause excessive disturbances to the entire MTDC system.

6. Conclusion

This study investigates the interoperability between the classical PI controller and advanced MPC, BSC, and STSMC controllers during large transients of future MTDC systems. First, the general MMC dynamics and its $\Sigma - \Delta$ representation are illustrated. Second, detailed modeling processes of different controllers and the control gain parameters are given. After that, this article introduces the constructions of the tested MTDC system in the RTDS environment, including detailed information on the RTDS racks/GTFPGA units, submarine cables, wind turbines, DC protection, and circuit breakers. In the end, an interoperability investigation was conducted for eight scenarios under four different system transients.

These findings are important for achieving interoperability between different controllers. Control capabilities under system transients vary from different control allocations. Generally, the scenarios with non-linear controllers show better transient performance by achieving faster settling time and fewer variations of DC voltage and active power. The insights from numerical results may assist in establishing the optimal controller allocation under each system oscillation scenario. On the whole, the findings of this study have many important implications for constructing multi-vendor HVDC grids in future industrial practice.

Continued efforts are needed to extend this work in four directions:

1. Smooth the undesired power oscillation when the controller of MMC3 switches from BSC to STSMC.
2. Conduct research on the mathematical mechanism of the interaction between different controllers.
3. Enhance the control strategy to mitigate the broadband oscillation in the VSC-HVDC system.
4. Develop the centralized layer of MMMC controllers with traditional and advanced controllers on MTDC system.

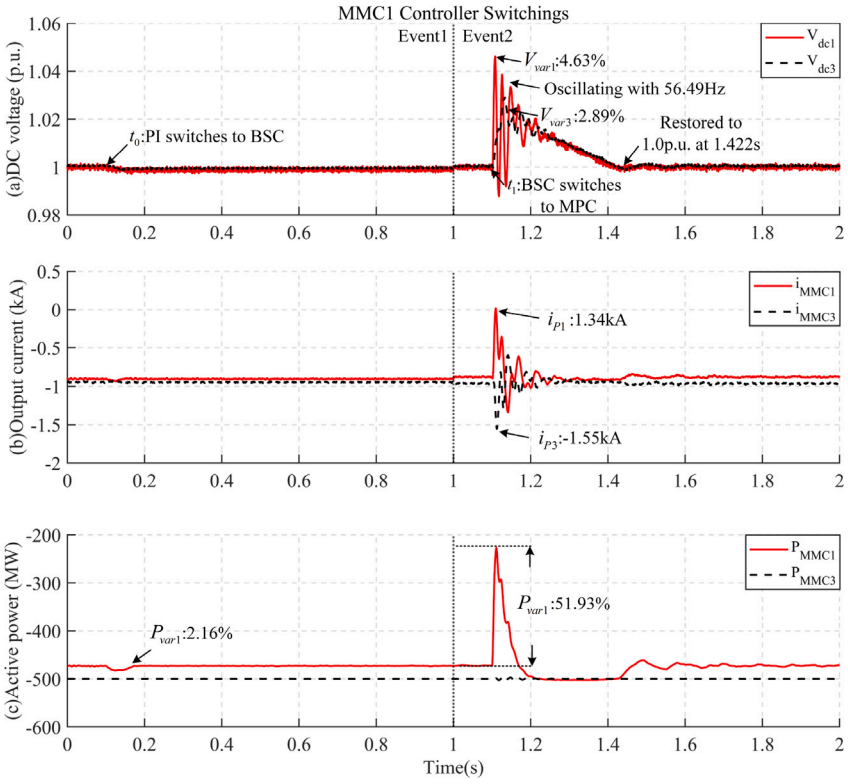

Fig. 14. Simulation of case V: (a) DC voltage. (b) Output current. (c) Active power.

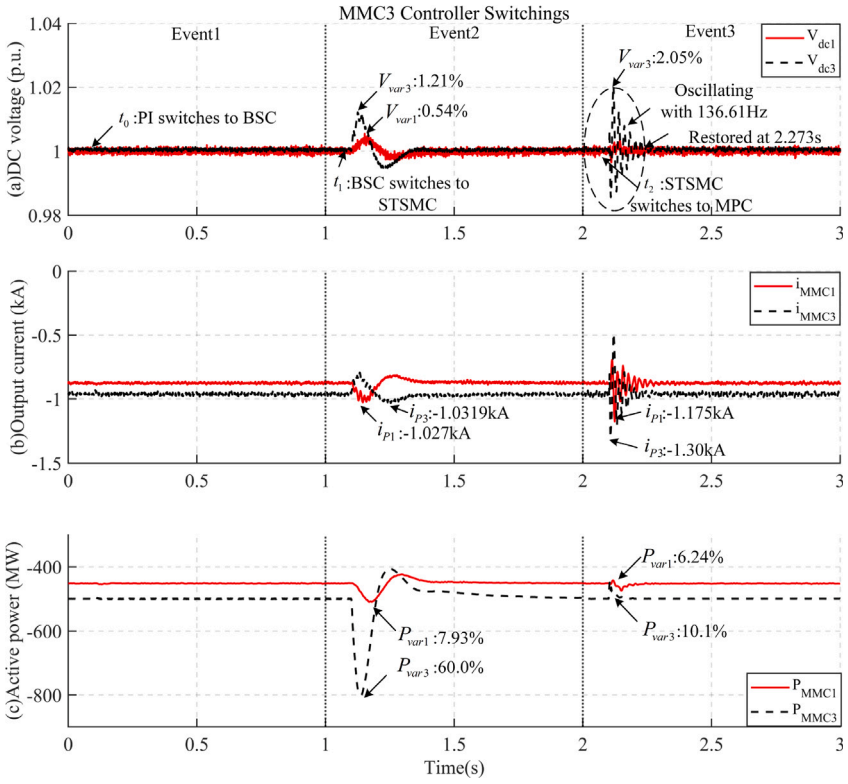

Fig. 15. Simulation of case V: (a) DC voltage. (b) Output current. (c) Active power.

CRediT authorship contribution statement

Le Liu: Conception and design of study, Acquisition of data, Analysis and/or interpretation of data, Writing – original draft, Writing – review & editing. **Ajay Shetgaonkar:** Conception and design of study, Acquisition of data. **Aleksandra Lekić:** Conception and design of study, Analysis and/or interpretation of data, Writing – original draft, Writing – review & editing.

Declaration of competing interest

The authors declare that they have no known competing financial interests or personal relationships that could have appeared to influence the work reported in this paper.

Data availability

No data was used for the research described in the article.

Acknowledgment

The authors would like to thank Prof. M. Popov for his generous support and encouragement. All authors approved the version of the manuscript to be published.

References

[1] European network of transmission system operators for electricity ENTSO-e position on offshore development interoperability. 2021.
[2] Wickramasinghe HR, Konstantinou G. Interoperability of modular VSC topologies in multi-converter multiterminal DC systems. Electr Power Syst Res 2021;196:107225.
[3] Rault P, Despouys O, Petit A, Saad H, Vozikis D, Gao S, Freytes J, Narayanan M, Ramet M, Zeller M, Askvid P. Implementation of a dedicated control to limit adverse interaction in multi-vendor HVDC systems. In: 15th IET international conference on ac and dc power transmission. 2019, p. 1–6.
[4] Ansari JA, Liu C, Khan SA. MMC based MTDC grids: A detailed review on issues and challenges for operation, control and protection schemes. IEEE Access 2020;8:168154–65.
[5] Wang M, Leterme W, Chaffey G, Beerten J, Van Hertem D. Multi-vendor interoperability in HVDC grid protection: State-of-the-art and challenges ahead. IET Gener Transmiss Distrib 2021;15(15):2153–75.
[6] Paths B. WP9: Final recommendations for interoperability of multivendor hvdc systems. 2018, D9.3.
[7] Chaffey G, Leterme W, Van Hertem D, Adeuyi O, Cowan I, Ponnalagan B, Rahman MH, Jahn I, Ishida-san K, Kunjumuhammed L, Page F. D9. 1– Real-time models for benchmark DC grid systems. 2018.
[8] WG b4.72, DC grid benchmark models for system studies, (June). 2020, p. 1–270.
[9] CIGRE working group B4.76, DC-DC converters in HVDC grids and for connections to HVDC systems, March. 2021, p. 1–196.
[10] IEEE. Stability definitions and characterization of dynamic behavior in systems with high penetration of power electronic interfaced technologies. Pes-Tr77, April, 2020, p. 1–42.
[11] Bergna-Diaz G, Freytes J, Guillaud X, D'Arco S, Suul JA. Generalized voltage-based state-space modeling of modular multilevel converters with constant equilibrium in steady state. IEEE J Emerg Sel Top Power Electron 2018;6(2):707–25.
[12] Shetgaonkar A, Lekić A, Rueda Torres JL, Palensky P. Microsecond enhanced indirect model predictive control for dynamic power management in MMC units. Energies 2021;14(11).
[13] Karamanakos P, Liegmann E, Geyer T, Kennel R. Model predictive control of power electronic systems: Methods, results, and challenges. IEEE Open J Indust Appl 2020;1:95–114.
[14] McNamara P, Milano F. Model predictive control-based AGC for multi-terminal HVDC-connected ac grids. IEEE Trans Power Syst 2018;33(1):1036–48.
[15] Moon J-W, Gwon J-S, Park J-W, Kang D-W, Kim J-M. Model predictive control with a reduced number of considered states in a modular multilevel converter for HVDC system. IEEE Trans Power Deliv 2015;30(2):608–17.
[16] Ahmadijokani M, Mehrasa M, Sleiman M, Sharifzadeh M, Sheikholeslami A, Al-Haddad K. A back-stepping control method for modular multilevel converters. IEEE Trans Ind Electron 2021;68(1):443–53.
[17] Jin Y, Xiao Q, Jia H, Mu Y, Ji Y, Teodorescu R, Dragičević T. A dual-layer back-stepping control method for Lyapunov stability in modular multilevel converter based STATCOM. IEEE Trans Ind Electron 2022;69(3):2166–79.
[18] Liu Z, Xie S, Kang Y. Disturbance-tracking-based backstepping control for VSC-HVDC systems with mismatched uncertainties. In: 2020 12th IEEE PES asia-pacific power and energy engineering conference. 2020, p. 1–5.
[19] Zhao X, Li K. Adaptive backstepping droop controller design for multi-terminal high-voltage direct current systems. IET Gener Transmiss Distrib 2015;9(10):975–83.
[20] Sadeghi R, Madani SM, Ataei M, Agha Kashkooli MR, Ademi S. Super-twisting sliding mode direct power control of a brushless doubly fed induction generator. IEEE Trans Ind Electron 2018;65(11):9147–56.
[21] Lascu C, Argeseanu A, Blaabjerg F. Supertwisting sliding-mode direct torque and flux control of induction machine drives. IEEE Trans Power Electron 2020;35(5):5057–65.
[22] Cigré WG. B4. 57."Guide for the development of models for HVDC converters in a HVDC grid". CIGRE Technical Brochure 2014;604.
[23] Wachal R, Jindal A, Dennetiere S, Saad H. HVDC converters in a HVDC grid. CigrÉ Working Group B4.57. 2014.
[24] Cigré WG. B4. 72."DC grid benchmark models for system studies". CIGRE Technical Brochure 2020;804.
[25] Shetgaonkar A, Liu L, Lekić A, Popov M, Palensky P. Model predictive control and protection of MMC-based MTDC power systems. Int J Electr Power Energy Syst 2023;146:108710.
[26] Wang L. Model predictive control system design and implementation using MATLAB®. Springer Science & Business Media; 2009.
[27] Liu L, Lekić A, Popov M. Robust adaptive back-stepping control approach using quadratic Lyapunov functions for MMC-based HVDC digital twins. In: International symposium on leveraging applications of formal methods. Springer; 2022, p. 126–38.
[28] RTDS Technologies Inc. VSC small time-step turorial of RTDS user manuals. 2013, p. 4–48.
[29] Maguire T, Warkentin B, Chen Y, Hasler J. Efficient techniques for real time simulation of MMC systems. In: Proc. Int. Conf. Power Syst. Transients. 2013, p. 1–7.
[30] Matar M, Paradis D, Iravani R. Real-time simulation of modular multilevel converters for controller hardware-in-the-loop testing. IET Power Electron 2016;9(1):42–50.
[31] Weather file. 2022, https://weatherfile.com/ Accessed 08 December 2021.
[32] Liu L, Liu Z, Popov M, Palensky P, van der Meijden MAMM. A fast protection of multi-terminal HVDC system based on transient signal detection. IEEE Trans Power Deliv 2021;36(1):43–51.
[33] Tong N, Tang Z, Wang Y, Lai CS, Lai LL. Semi AI-based protection element for MMC-MTDC using local-measurements. Int J Electr Power Energy Syst 2022;142:108310.
[34] Wang D, Liu H, Zhang D, Qiao F, Liu X, Hou M. Travelling wave fault location for LCC–MMC–MTDC transmission lines based on frequency-dependent characteristic. Int J Electr Power Energy Syst 2022;138:107863.
[35] Zhang C, Song G, Wang T, Dong X. An improved non-unit traveling wave protection method with adaptive threshold value and its application in HVDC grids. IEEE Trans Power Deliv 2020;35(4):1800–11.
[36] Liu S, Popov M, Mirhosseini SS, Nee S, Modeer T, Ängquist L, Belda N, Koreman K, van der Meijden MAMM. Modeling, experimental validation, and application of VARC HVDC circuit breakers. IEEE Trans Power Deliv 2020;35(3):1515–26.